ANTIOXIDANTS & REDOX SIGNALING
Volume 37, Numbers 13–15, 2022

DOI: 10.1089/ars.2021.0133

ORIGINAL RESEARCH COMMUNICATION

Enduring Reactive Oxygen Species Emission Causes Aberrant Protein S-Glutathionylation Transitioning Human Aortic Valve Cells from a Sclerotic to a Stenotic Phenotype

Vincenza Valerio,[1,2] Gizem Keceli,[3,*] Donato Moschetta,[1,4,*] Benedetta Porro,[1] Michele Ciccarelli,[5] Ilaria Massaiu,[1] Paola Songia,[1] Angela S. Maione,[1] Valentina Alfieri,[1] Veronika A. Myasoedova,[1] Marco Zanobini,[1] Nazareno Paolocci,[3,6] and Paolo Poggio[1]

Abstract

Aims: During calcific aortic valve stenosis (CAVS) progression, oxidative stress and endothelial dysfunction mark the initial pathogenic steps with a parallel dysregulation of the antioxidant systems. Here, we tested whether oxidation-induced protein S-glutathionylation (P-SSG) accounts for a phenotypic switch in human aortic valvular tissue, eventually leading to calcium deposition. Next, we tested whether countering this reactive oxygen species (ROS) surge would prevent these perturbations.

Results: We employed state-of-the-art technologies, such as electron paramagnetic resonance (EPR), liquid chromatography-tandem mass spectrometry, imaging flow-cytometry, and live-cell imaging on human excised aortic valves and primary valve endothelial cells (VECs). We observed that a net rise in EPR-detected ROS emission marked the transition from fibrotic to calcific in human CAVS specimens, coupled to a progressive increment in P-SSG deposition. In human VECs (hVECs), treatment with 2-acetylamino-3-[4-(2-acetylamino-2-carboxyethylsulfanylthiocarbonylamino)phenylthiocarbamoylsulfanyl]propionic acid triggered highly oxidizing conditions prompting P-SSG accumulation, damaging mitochondria, and inducing endothelial nitric oxide synthase uncoupling. All the events conjured up in morphing these cells from their native endothelial phenotype into a damaged calcification-inducing one. As proof of principle, the use of the antioxidant N-acetyl-L-cysteine prevented these alterations.

Innovation: Borne as a compensatory system to face excessive oxidative burden, with time, P-SSG contributes to the morphing of hVECs from their innate phenotype into a damaged one, paving the way to calcium deposition.

Conclusion: Our data suggest that, in the human aortic valve, unremitted ROS emission along with a P-SSG build-up occurs and accounts, at least in part, for the morphological/functional changes leading to CAVS. *Antioxid. Redox Signal*. 37, 1051–1071.

Keywords: calcific aortic valve stenosis, endothelial cells, oxidative stress, protein S-glutathionylation, antioxidants, calcification

[1]Unità per lo Studio delle Patologie Aortiche, Valvolari e Coronariche, Centro Cardiologico Monzino IRCCS, Milan, Italy.
[2]Dipartimento di Medicina Clinica e Chirurgia, Università degli Studi di Napoli Federico II, Napoli, Italy.
[3]Division of Cardiology, Department of Medicine, Johns Hopkins University School of Medicine, Baltimore, Maryland, USA.
[4]Dipartimento di Scienze Farmacologiche e Biomolecolari, Università degli Studi di Milano, Milano, Italy.
[5]Dipartimento di Medicina, Chirurgia e Odontoiatria, Università degli Studi di Salerno, Baronissi, Italy.
[6]Department of Biomedical Sciences, University of Padova, Padova, Italy.
*These authors contributed equally to this work.

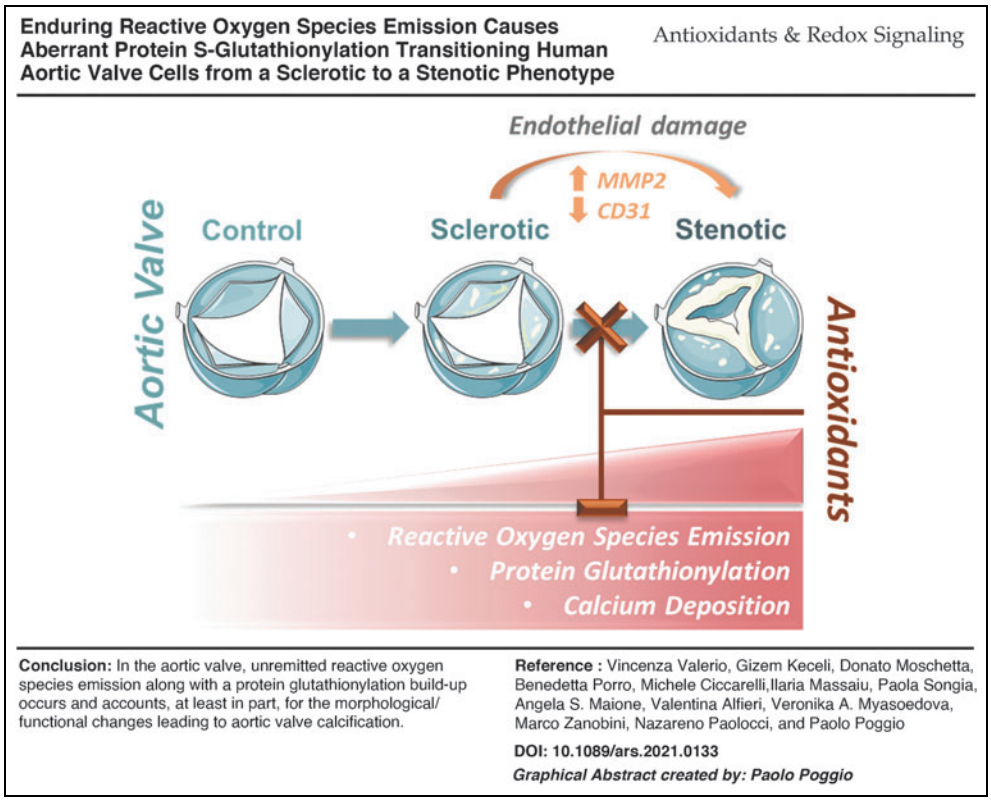

Introduction

Calcific aortic valve stenosis (CAVS) is the most common heart valve pathological condition worldwide (1). The CAVS is age-related (45), with a prevalence of almost 3% in the general population older than 65 years (51). The disease's natural history evolves from an initial asymptomatic phase characterized by a thickening of the leaflets bearing possible micro-calcifications and a preserved left ventricle outflow tract still (24).

This condition, known as aortic valve sclerosis (AVSc), has a prevalence of about 30% in adults older than 65 years of age (26). About 10% of these cases morph into aortic stenosis (AS), displaying massive calcifications and overt hemodynamic impairment (52). The only therapeutic option available for AS patients is surgery or transcatheter aortic valve replacement (AVR) (7). Therefore, penetrating CAVS pathogenic mechanisms would pave the way to new treatment opportunities and reduce its socioeconomic burden.

Innovation

Calcific aortic valve stenosis remains a challenging clinical condition and factor accounting for the valve leaflets' progressive remodeling, from fibrotic to calcific, elusive. Our study demonstrates that unremitted reactive oxygen species (ROS) emission from endothelial cells, along with a protein S-glutathionylation build-up, occurs and accounts, at least in part, for the morphological/functional changes occurring in the human aortic valves when they switch from a sclerotic to a stenotic phenotype, thus increasing the calcification chance. Our *in vitro* data suggest that it is possible to de-activate this mechanism, leveraging endogenous signaling or exogenous compounds that are able to counter ROS emission and MMP expression/activity.

The CAVS unfolding is a complex process entailing many different cell types (71). Valve interstitial cells (VICs), during CAVS progression, transdifferentiate and trigger the disruption of the extracellular matrix homeostasis, prompting calcium deposition (44). Alterations in valve endothelial cells (VEC) play a pivotal role in this process. Indeed, the endothelial dysfunction of the aortic valve leaflets is the ineludible first step of CAVS development and progression (66). Oxidative stress, stemming from an imbalance between reactive oxygen species (ROS) formation and scavenging, is one factor that chiefly accounts for this alteration (22, 32, 59).

The antioxidant armamentarium encompasses a battery of enzymatic and non-enzymatic activities tailored to maintain tissue/cell redox homeostasis (10). Among them, soluble glutathione is the primary non-enzymatic antioxidant system present in all cells' compartments, and the ratio between its reduced (GSH) and oxidized (GSSG) form typically serves to index tissue oxidative stress and redox status (3, 10).

However, when dysregulated, the glutathione system can contribute to the pathogenesis of several cardiovascular diseases, including hypertension, atherosclerosis, and aortic valve degeneration (20, 68). In the presence of highly

oxidizing conditions, redox-sensitive proteins involved in many, if not all, cell functions may undergo post-translational modifications, including protein S-glutathionylation (P-SSG) (28).

This reversible modification consists of the interaction between molecules of GSH and/or GSSG with susceptible cysteine residues of proteins (55). P-SSG has been found in various structural and functional proteins, including actin (28), modifying their characteristics and functions (27). P-SSG can be part of many alterations affecting signaling mechanisms at the foundation of different cardiovascular disorders, serving as an early biomarker of pathological conditions (50). A progressive rise in the pro-oxidative milieu intervenes in the human valvular tissue during CAVS involution toward stenosis (22).

However, direct specific quantification of ROS emission from human aortic valve leaflets is lacking. At the same time, previous reports relied on the evidence that both superoxide dismutase and catalase are downregulated in CAVS (11, 43). Regardless of this, no reports have yet tested whether the ROS burden eventually varies with the disease stages, along with the possible role of P-SSG post-translational modification in the CAVS disease progression.

Therefore, we designed the present study to test three main outstanding hypotheses. First, we aim at determining whether an unremitted ROS emission from valve tissues underscores the sclerotic-to-stenotic switch in human CAVS, leading to a P-SSG build-up. Second, we tested whether this alteration, in turn, prompts endothelial damage, causing morphological/functional changes of VECs, ultimately promoting calcium deposition. Finally, we assessed whether preventing this ROS surge and P-SSG maladaptive response *via* an exogenous thiol compound prevents this sclerosis-to-stenosis transition and, ultimately, calcification in human VECs (hVECs).

Results

Increased ROS emission and P-SSG mark the transition from sclerosis to stenosis in human aortic valves

Oxidative stress may herald CAVS onset and progression (22). However, no data are available regarding specific quantification of ROS emission from human aortic valve leaflets at different disease stages. To fill this gap, we used an electron paramagnetic resonance (EPR) approach that is the only method for the direct detection of paramagnetic species, such as ROS (13). We employed this approach in aortic valve specimens obtained from three different patient populations, that is, control subjects and patients with aortic sclerosis or AS (see patients' enrollment description). A one-way ANOVA analysis revealed significant differences between the three groups (ANOVA $p = 0.004$; p-trend $= 0.001$).

In detail, AS samples displayed a striking rise in ROS levels over controls ($91.5.1 \pm 20.7$ *vs.* 21.0 ± 4.3 arbitrary units (AU), respectively; $p = 0.003$; Fig. 1a–c). However, aortic sclerosis specimens (56.9 ± 12.2 AU), being an intermediate stage of CAVS, were not statistically significant from control or AS ones ($p = 0.16$). This evidence attests that an increment in valve ROS emission accompanies human CAVS disease progression.

Next, we interrogated whether P-SSG and deregulation of glutathione reductase (GR), one of the enzymes involved in GSH regeneration, parallel the escalation in valve ROS emission, and whether they affect aortic valve tissue biology and function. To this end, we measured P-SSG levels in whole tissue extracts that include proteins from both interstitial and endothelial valve cell types (*i.e.,* VICs and VECs). We found significant differences between the three groups (ANOVA $p = 0.02$; p-trend $= 0.007$).

More specifically, aortic samples from AS patients displayed substantially more elevated P-SSG levels than control subjects ($\log2FC = +0.3 \pm 0.09$; $p = 0.02$; Fig. 1d, e). Of note, sclerotic samples did not differ from control or stenotic samples. In parallel, immunohistochemistry analysis showed no difference in the expression of GR at tissue level at different stages of pathology (Supplementary Fig. S1). This data set suggests ROS emission and P-SSG as a new possible signature of aortic valve disease progression toward stenosis.

Blocking GR boosts ROS emission and P-SSG in porcine VECs

We employed an *in vitro* model of aberrant aortic valve P-SSG by using porcine VECs (pVEC) to get mechanistic insights into P-SSG-induced changes in endothelial cells. To this end, we used 2-acetylamino-3-[4-(2-acetylamino-2-carboxyethylsulfanylthiocarbonylamino)phenylthiocarbamoylsulfanyl]propionic acid (2-AAPA) to disrupt cells' ability to detoxify ROS, leading to increased intracellular oxidative stress, thus enhancing P-SSG formation chance. Figure 2a and b reveals that 2-AAPA treatment significantly augmented P-SSG levels (ANOVA; $p < 0.0001$).

In greater detail, we observed that, compared with untreated and DMSO control conditions, the compound ($50\ \mu M$) led to a sizable increment in P-SSG ($\log2FC = +5.3 \pm 1.0$; $p = 0.0001$). Moreover, consistent with previous studies (68), the P-SSG positive bands had the same molecular weight as β-actin, which could result in an altered ratio between soluble and polymerized protein, leading to significant cell architecture perturbations (70). We also noticed a marked rise in the phosphorylated form of the histone H2AX (γH2AX; ANOVA $p = 0.001$; Supplementary Fig. S2), thus denoting the presence of foci of DNA repair due to double-strand brakes.

This effect was dose-dependent (p-trend <0.0001). Indeed, pVECs treated with different concentrations of 2-AAPA (50, 75, and $100\ \mu M$) led to significant escalating γH2AX levels when compared with untreated cells ($\log2FC = +2.6 \pm 0.8$; $\log2FC = +2.6 \pm 0.7$; $\log2FC = +3.0 \pm 0.4$, respectively; all $p < 0.05$). Since 2-AAPA at $50\ \mu M$ was the minimum effective dose able to induce P-SSG and DNA damage, we next interrogated whether or not this concentration imbalanced ''VECs'' redox status. To this end, we measured ROS production *via* a validated colorimetric assay.

As shown in Figure 2c–e, the cytofluorimetric analysis showed that 2-AAPA triggered a sizable ROS production compared with cells treated with DMSO ($26.2\% \pm 4.8\%$ *vs.* $13.9\% \pm 4.4\%$, respectively; $p = 0.04$). Hand in hand with this finding, the MTT assay revealed that treating pVECs with 2-AAPA abated cell viability drastically (ANOVA $p < 0.001$; Supplementary Fig. S3). Finally, we sought to determine whether adding N-acetyl-L-cysteine (NAC) would reduce/prevent the extent of this post-translational modification in

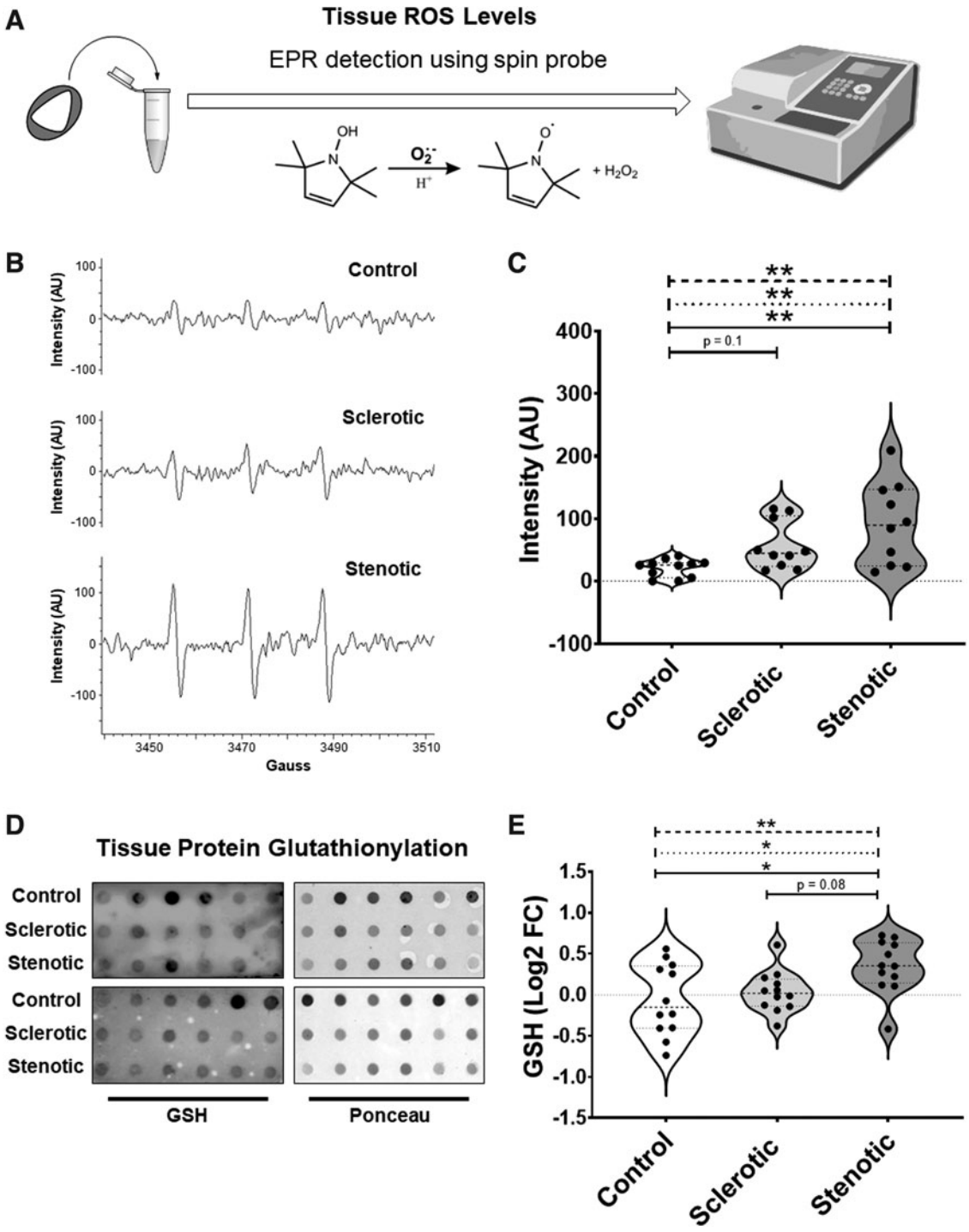

FIG. 1. ROS levels and P-SSG during calcific aortic valve stenosis progression. **(A)** Scheme showing EPR performed using a spin probe that reacts with extra- and intracellular oxygen free radicals to generate the detectable EPR. **(B)** EPR representative spectra for Control, Sclerotic, and Stenotic tissue samples. **(C)** Violin plot representing EPR quantification. (Control = 11; Sclerotic = 10; Stenotic = 10). **(D)** *Dot blot* representative images of P-SSG in whole extracts of aortic valve leaflets at different stages of the pathology. **(E)** Violin plot representing *dot blot* relative quantification by ImageJ. (Control = 12; Sclerotic = 12; Stenotic = 12) $^{**}p \leq 0.01$; $^{*}p < 0.05$; *dashed line*: Test for trend; *dotted line*: ANOVA; *solid line*: Tukey post-test. EPR, electron paramagnetic resonance; P-SSG, protein S-glutathionylation; ROS, reactive oxygen species.

pVECs. We found that NAC (2 m*M*) supplementation, before and during 2-AAPA administration, substantially attenuated P-SSG deposition compared with 2-AAPA treatment alone (log2FC = +1.5 ± 1.1 *vs.* +5.2 ± 1.0, respectively; $p = 0.01$; Fig. 2f, g).

We interpret these findings to indicate that blocking GR and thioredoxin activity in pVECs *via* 2-AAPA is sufficient to build up P-SSG in a sizable and likely functionally relevant manner, as suggested by the earlier reported decrement in VECs' viability and mounting oxidative stress.

During CAVS progression, hVECs acquire resilience against oxidative stress

Next, we interrogated whether changes in the ratio between GSH (*i.e.,* reduced glutathione) and GSSG (*i.e.,* oxidized glutathione), a typical metric of oxidative stress in cells, occur in diseased aortic leaflets and whether these alterations are stage-dependent in hVEC due to progressive increments in P-SSG, as mentioned earlier. We used a state-of-the-art methodology to monitor the GSH/GSSG ratio, such as liquid chromatography-tandem mass spectrometry (LC-MS/MS) (68).

In healthy endothelial cells, this ratio typically ranges around 100:1; however, in many pathological conditions and oxidative stress models, this ratio has been shown to decrease to 10:1 or even 1:1 (74, 75). Intriguingly, in hVECs at a different stage of CAVS, we noticed a progressive rise in the GSH/GSSG ratio, escalating with disease worsening. Indeed, group analysis revealed significant differences between the CAVS stages (ANOVA $p = 0.0003$; Fig. 3a) with an increment during disease progression (p-trend <0.0001).

We also found that sclerotic hVECs had a significantly higher GSH/GSSG ratio than control cells (211.3 ± 16.8 *vs.* 65.3 ± 17.2, respectively; $p = 0.01$). However, stenotic hVECs displayed the highest GSH/GSSG ratio (306.4 ± 50.0; $p = 0.0002$ *vs.* the control group). Separate analyses of GSH and GSSG showed that, intriguingly and unexpectedly, stenotic hVECs have higher GSH bioavailability than the control group (45.6 ± 4.5 *vs.* 21.6 ± 6.0, respectively; $p = 0.0002$; Supplementary Fig. S4a) and at the same time lower GSSG presence than controls (0.1 ± 0.01 *vs.* 0.3 ± 0.02 respectively; $p = 0.008$; Supplementary Fig. S4b).

Therefore, the stenotic hVECs appear to be more resilient against oxidative stress, thus probably less prone to P-SSG induction. First, we induced oxidative stress by using 2-AAPA treatment to test this intriguing possibility. In control hVECs, this oxidative challenge led to a drastic (85%) decrease in the GSH/GSSG ratio compared with untreated ($p = 0.005$) and DMSO conditions ($p = 0.02$; Fig. 3b). The same substantial drop was overt in sclerotic hVECs in which the ratio declined by 82% and 59% compared with -untreated ($p < 0.0001$) and DMSO-treated cells ($p = 0.001$), respectively (Fig. 3c).

Conversely, in stenotic hVECs, we captured a less pronounced decline (36%) in the GSH/GSSG ratio after 2-AAPA treatment compared with untreated stenotic ones ($p = 0.052$; Fig. 3d). At the same time, no sizable difference was noted compared with DMSO-treated cells. We interpret these findings to indicate that, owing to a higher basal GSH/GSSG ratio (Fig. 3a), due to a higher basal GSH (Supplementary Fig. S4a) and smaller GSSG rise (Supplementary Fig. S4b) after 2-AAPA treatment, the stenotic hVECs are more protected against further oxidative insults (Supplementary Fig. S4c).

Second, regarding P-SSG, we did not find any basal difference among hVECs at the three pathological stages considered ($p = 0.505$). Notwithstanding, we noticed induction of this post-translational modification after 2-AAPA treatment in all three hVECs groups (Fig. 4a–c and Supplementary Fig. S5). In particular, in control hVECs, P-SSG drastically increased after 2-AAPA treatment (log2FC = $+2.3 \pm 0.6$; $p < 0.01$) compared with -untreated and DMSO-treated ones (Fig. 4a).

In sclerotic hVECs, we noticed a similar P-SSG rise (log2FC = $+2.1 \pm 0.6$; $p < 0.01$; Fig. 4b). Conversely, in stenotic hVECs, the P-SSG increment was less manifest (log2FC = 0.7 ± 0.2; $p < 0.05$; Fig. 4c). To validate that stenotic hVECs are more resistant to oxidative stress than control and sclerotic cells, we tested the extent of 2-AAPA-induced cell apoptosis and viability. As shown in Figure 4d–g, we highlighted the presence of early apoptosis after 2-AAPA treatment compared with DMSO, in control ($+13.3\% \pm 1.5\%$; $p = 0.0003$ Fig. 4d, e), sclerotic ($+23.62\% \pm 7.2\%$; $p = 0.02$; Fig. 4d, f), and stenotic ($+22.75\% \pm 4.0\%$; $p = 0.002$; Fig. 4d, g) hVECs.

However, after 2-AAPA treatment, a slight increase in late apoptosis was detected only in stenotic hVECs ($+2.8 \pm 0.7$, $p = 0.01$; Fig. 4d, g). Further, to confirm the activation of the apoptotic pathway and understand which apoptotic cascade was activated, we profiled 35 apoptosis-related proteins in stenotic cell lysates (Supplementary Fig. S5b, c). The 2-AAPA treatment induced a significant overexpression of the active form of caspase 3 (Cleaved Casp3), of heme oxygenase 1 (HO-1/HMOX1/HSP32), and of heat shock protein 60 (HSP60).

In particular, after 2-AAPA treatment, the cleaved Casp3 increased by 25% (Supplementary Fig. S5d; DMSO Integrated Density (ID) = 0.08 ± 0.008 and 2-AAPA ID = 0.1 ± 0.02; $p = 0.02$) and, in relation to its inactive form (procaspase), by 50% (Supplementary Fig. S5e; Ratio cleaved Casp3/Pro casp3 ID in DMSO = 0.1 ± 0.01 and in 2-AAPA ID = 0.2 ± 0.03; $p = 0.01$) with a concomitant overexpression of HO-1 (Supplementary Fig. S5f; DMSO ID = 0.09 ± 0.01 and 2-AAPA ID = 0.2 ± 0.01; $p = 0.001$).

Indeed, the co-presence of cleaved caspase and HSP60 protein confirms the activation of the apoptotic process and

FIG. 2. *In vitro* model of P-SSG in pVECs. (A) GSH and β-actin Western blot representative images of pVEC after 4 h of treatment with DMSO and increasing concentrations of 2-AAPA and 24 h of recovery. GSH is shown in *green*, and β-actin is shown in *red*. (U = Untreated, $n = 6$; D = DMSO, $n = 5$; 12.5 = 2-AAPA 12.5 μM, $n = 5$; 25 = 2-AAPA 25 μM, $n = 5$; 50 = 2-AAPA 50 μM, $n = 6$; 75 = 2-AAPA 75 μM, $n = 6$; 100 = 2-AAPA 100 μM $n = 6$) **(B)** Scatter plot with bar of Western blot relative quantification performed with ImageJ. **(C, D)** Image flow cytometry analysis of ROS levels in pVECs treated with DMSO and 2-AAPA 50 μM (40×). **(E)** Scatter plot with bar showing the percentage of pVECs positive cells after 2-AAPA 50 μM treatment and 24 h of recovery ($n = 3$). **(F)** Western blot representative images of β-actin S-glutathionylation when pVECs are treated with NAC before and during 2-AAPA 50 μM treatment. GSH is shown in *green*, and β-actin is shown in *red*. (U = Untreated; D = DMSO; 50 = 2-AAPA 50 μM; N = NAC 2 mM; N+D = NAC 2 mM + DMSO; N + 50 = NAC 2 mM + 2-AAPA 50 μM). **(G)** Scatter plot with bar representing Western blot relative quantification performed with ImageJ. ***$p \le 0.001$; **$p \le 0.01$;*$p \le 0.05$; *dotted line*: ANOVA; *solid line*: Tukey post-test ($n = 6$). NAC, N-acetyl-L-cysteine; pVEC, porcine valve endothelial cell.

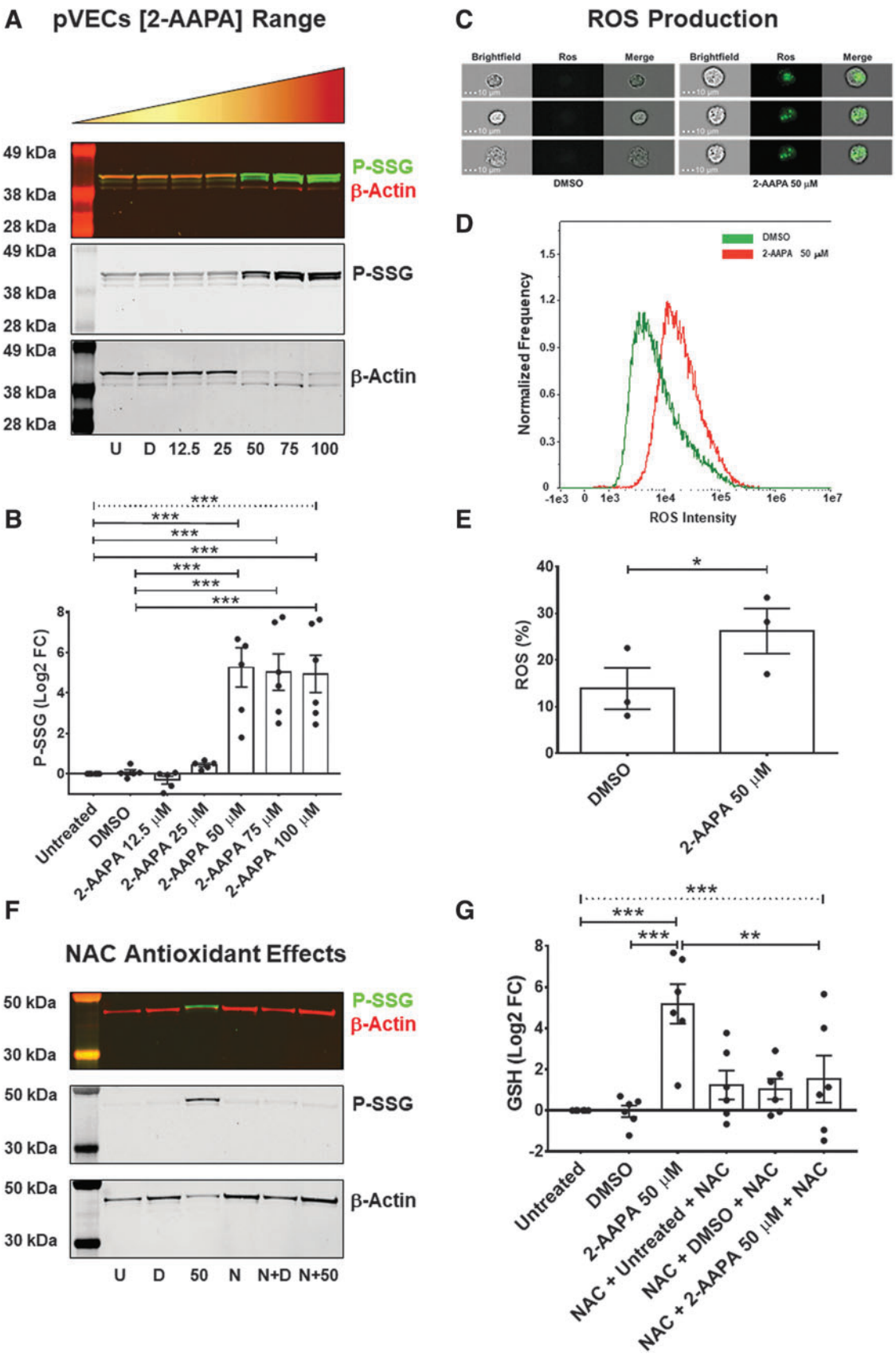
A
pVECs [2-AAPA] Range
49 kDa
38 kDa
28 kDa
P-SSG
β-Actin
U D 12.5 25 50 75 100
B
P-SSG (Log2 FC)
Untreated
DMSO
2-AAPA 12.5 μM
2-AAPA 25 μM
2-AAPA 50 μM
2-AAPA 75 μM
2-AAPA 100 μM
C
ROS Production
Brightfield
Ros
Merge
DMSO
2-AAPA 50 μM
D
Normalized Frequency
ROS Intensity
E
ROS (%)
F
NAC Antioxidant Effects
50 kDa
30 kDa
U D 50 N N+D N+50
G
GSH (Log2 FC)
NAC + Untreated + NAC
NAC + DMSO + NAC
NAC + 2-AAPA 50 μM + NAC

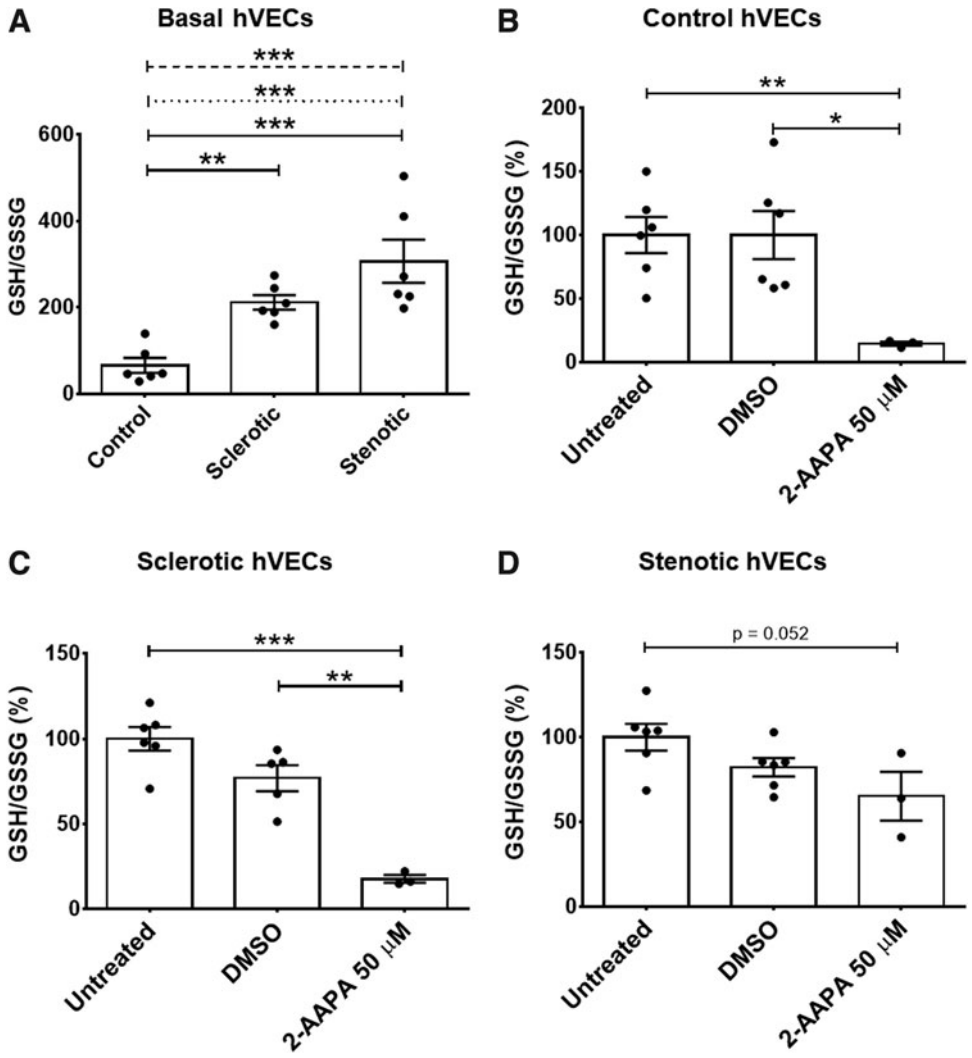

FIG. 3. Imbalance of glutathione system during calcific aortic valve stenosis progression in hVECs. (A) Scatter plot with bar representing the ratio between reduced (GSH) and oxidized (GSSG) form of glutathione in hVEC at steady state. (Control $n=6$; Sclerotic $n=6$; Stenotic $n=6$) $***p\leq0.001$; $**p\leq0.01$; $*p\leq0.05$; *dashed line* = Test for trend; *dotted line*: ANOVA; *solid line*: Tukey post-test **(B–D)** Scatter plots with bar showing the percentage of GSH/GSSG ratio after 4 h of DMSO or 2-AAPA 50 μM and 24 h of recovery in control, sclerotic, and stenotic hVECs (Untreated $n=6$; DMSO $n=6$; 2-AAPA 50 μM $n=3$). *t*-test: $***p\leq0.001$; $**p\leq0.01$; $*p\leq0.05$. hVEC, human valve endothelial cell.

suggests the presence of potential mitochondrial damage (36). On the other hand, the overexpression of HSP60 (Supplementary Fig. S5; DMSO ID = 0.1 ± 0.02 and 2-AAPA = 0.3 ± 0.03; $p=0.004$) further confirms the presence of oxidative stress since the cells' attempt to react to the insult caused by oxidative stress status (49).

At the same time, assessing cell viability after 2-AAPA treatment, we noticed that control and sclerotic hVECs exhibited a drastic drop in viability rate *versus* DMSO-treated ones (control hVECs = −60.1% ± 10.2%, $p=0.0002$ *vs.* DMSO; Fig. 4h; sclerotic hVECs = −65.7% ± 2.3%, $p<0.0001$ *vs.* DMSO; Fig. 4i). However, after 2-AAPA treatment, stenotic hVECs displayed a modest decline in viability compared with DMSO (−44.0% ± 8.5%, $p=0.001$; Fig. 4j) as well as *versus* controls and sclerotic ones (Supplementary Fig. S6). These data collectively suggest that those endothelial cells that survived during CAVS progression over the years harnessed adaptive/compensatory mechanisms, such as boosted antioxidant systems, including the glutathione one.

Protein glutathionylation favors endothelial morphological/functional changes in hVECs

The earlier reported findings suggest that, despite an acquired resistance against oxidative stress, hVECs undergo

FIG. 4. hVECs *in vitro* P-SSG effects on apoptosis and survival rate in hVECs. (A–C) Scatter plots with bar of Western blot relative quantification performed by ImageJ. (Control: Untreated $n=4$; DMSO $n=4$; 2-AAPA 50 μM $n=4$; 2-AAPA 100 μM $n=3$; Sclerotic: Untreated $n=5$; DMSO $n=4$; 2-AAPA 50 μM $n=5$; 2-AAPA 100 μM $n=5$; Stenotic: Untreated $n=5$; DMSO $n=5$; 2-AAPA 50 μM $n=5$; 2-AAPA 100 μM $n=4$). $**p\leq0.01$; $*p\leq0.05$; *dashed line* = Test for trend; *dotted line*: ANOVA; *solid line*: Tukey post-test. **(D)** Scatter plot representing cytofluorimetric analysis of Annexin V (Ann V) and Propidium Iodide (PI) in control ($n=6$), sclerotic ($n=6$), and stenotic ($n=6$) hVECs after DMSO (upper scatter plots) or 2-AAPA 50 μM (lower scatter plots) treatments. **(E–G)** Scatter plot with bar showing early apoptotic cells ($AnnV^+/PI^-$) and late apoptotic ($AnnV^+/PI^+$) $***p\leq0.001$; $**p\leq0.01$; $*p\leq0.05$ *t*-test. **(H–J)** Scatter plot with graph representing the percentage of viable cells after DMSO or 2-AAPA treatment in control ($n=6$), sclerotic ($n=6$), and stenotic ($n=6$) hVECs. $***p\leq0.001$; $**p\leq0.01$; *t*-test.

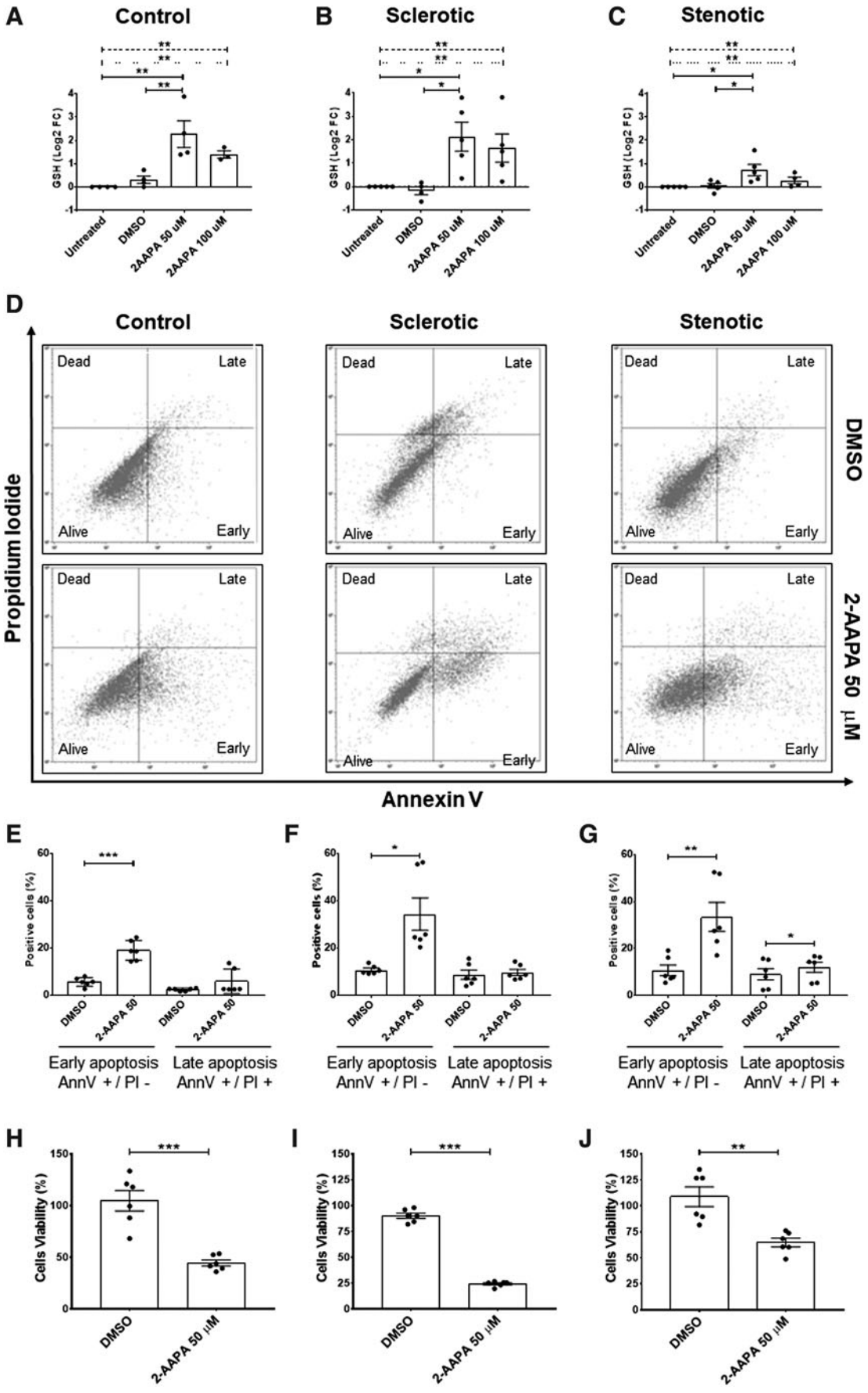
A
Control
B
Sclerotic
C
Stenotic
GSH (Log2 FC)
Untreated
DMSO
2AAPA 50 uM
2AAPA 100 uM
D
Control
Sclerotic
Stenotic
Dead
Late
Alive
Early
DMSO
2-AAPA 50 µM
Propidium Iodide
Annexin V
E
F
G
Positive cells (%)
DMSO
2-AAPA 50
Early apoptosis
AnnV + / PI -
Late apoptosis
AnnV + / PI +
H
I
J
Cells Viability (%)
DMSO
2-AAPA 50 µM

a profound structural (and likely functional) remodeling during CAVS progression. Therefore, we started dissecting possible mechanisms underlying these alterations by using an immunofluorescent staining approach. First, we observed that hVECs had the classical actin filament configuration under basal conditions (Fig. 5a top and middle panels).

In particular, in the 2D monolayer configuration, actin filaments were arranged below the plasma membrane, thus identifying the cortical actin and in the cytoplasm (56). However, after 2-AAPA treatments, we noticed salient morphological changes besides a P-SSG deposition rise (Fig. 5a lower panels). Namely, the cytoskeleton was de-structured with a predominant colocalization between glutathione and β-actin filaments, suggesting β-actin S-glutathionylation (negative staining control in Supplementary Fig. S7). Correspondingly, we found a significant fall in a specific endothelial marker, CD31 ($\log2FC = -1.6 \pm 0.3$; ANOVA $p < 0.0001$; Fig. 5b, c).

This fact suggests the loss of cell–cell junction and adhesion. Concomitantly, we found a significant increment in metalloproteinase type 2 (MMP2) active form (C-MMP2 $\log2FC = +0.53 \pm 0.2$; ANOVA $p = 0.03$; Fig. 5b, e). On the other hand, we also checked the expression of the tissue inhibitor of metalloproteinase 2 (TIMP2), a specific inhibitor of MMP2, and we observed a slight increase in this protein after 2-AAPA treatment only when compared with the untreated condition ($\log2FC = +0.5 \pm 0.2$; ANOVA $p = 0.02$; Fig. 5f).

Indeed, we noticed no difference in TIMP2 levels between DMSO and 2-AAPA treatment, and thus, MMP2 activation was not followed by a parallel rise in its endogenous inhibitor (*i.e.,* TIMP2). Since MMPs could directly influence cell surface proteins' expression (21), the MMP2 overexpression may help explain the loss of CD31. In aggregate, these data indicate that oxidative stress, inducing P-SSG, is conducive to morphological and functional changes.

Association between P-SSG and ROS emission via mitochondrial damage and endothelial nitric oxide synthase uncoupling in hVECs

Based on the earlier reported data, we measured ROS production in stenotic hVECs after the block of GR with 2-AAPA treatment, combining a colorimetric assay and cell live imaging. As shown in Figure 6a and b, ROS levels drastically increase after 2-AAPA treatment (ROS integrated density/confluence area DMSO $= 0.04 \pm 0.007$ *vs.* 2-AAPA $= 1.0 \pm 0.1$; $p < 0.0001$). In light of the increase in ROS emission and the upregulation of the HSP60 protein, an indicator of mitochondrial damage, we wondered whether the increase in ROS could stem from mitochondrial damage.

Therefore, *via* a state-of-the-art imaging flow cytometer evaluation, we observed a significant increase in the presence of mitochondrial damage in stenotic hVECs when treated with 2-AAPA (Mitosox positive cells %: $+44.8 \pm 7.9$; $p < 0.0001$ *vs.* DMSO; Fig. 6e).

In addition, since a notable ROS increment is driven by 2-AAPA, we speculated that this ROS surge could also derive from endothelial nitric oxide synthase (eNOS) uncoupling. In this regard, we checked the intracellular nitric oxide ($NO^{\cdot}$) levels and the concentration of the cofactor tetrahydrobiopterin (BH_4), known to be a critical determinant of eNOS activity and eNOS uncoupling (14), after blocking GR with 2-AAPA.

Thanks to live-cell imaging analysis and ELISA assay, we found a significant decrease in $NO^{\cdot}$ levels (2-AAPA $= 1.6 \pm 0.05$ *vs.* DMSO $= 1.8 \pm 0.04$; $p = 0.005$; Fig. 6f, g) with a concomitant decrease in BH_4 levels in cell lysates obtained from hVEC after 2-AAPA treatment when compared with DMSO (pg/mg: 66.7 ± 6.4 *vs.* 82.49 ± 3.1, respectively; $p = 0.01$; Fig. 6h). These findings indicate that mitochondrial damage and eNOS uncoupling concur in ROS rise, directly affecting endothelial, morphological, and functional changes.

NAC fends off P-SSG and consequent calcium deposition in hVECs

Aortic valve calcification is a stenotic CAVS signature, contributing to narrowing the aortic valve (48). Thus, we felt it necessary to determine whether excessive P-SSG deposition predisposes hVECs to calcification. To this purpose, we first evaluated the calcium deposition susceptibility of these cells after a challenge with a well-known calcification inducer (29). As expected, treatment with inorganic phosphate (Pi) caused significant hVECs calcification compared with untreated cells (47.3 ± 8.1 *vs.* 6.9 ± 1.0 ng of calcium/μg protein, respectively; $p = 0.0001$; Fig. 7a).

Then, we observed that the oxidative stress generated by 2-AAPA (50 μM) prompted hVECs calcification, differently from what occurred with DMSO alone (119.0 ± 16.1 *vs.* 8.7 ± 0.9 ng of calcium/μg protein, respectively; $p < 0.0001$; Fig. 7b). Finally, we proved that the addition of 2 mM NAC, 1 h before and during the 2-AAPA treatment, drastically lowered the calcium deposition ($-79.9\% \pm 8.1\%$; $p < 0.0001$) compared with hVECs treated with 2-AAPA alone.

This data set corroborates that oxidative stress *via* P-SSG plays a pivotal role in CAVS progression, inducing maladaptive mechanisms in hVECs, eventually leading to calcium deposition.

Discussion

Our study cements the view that escalating ROS emission in valve leaflets underscores the human CAVS involution

FIG. 5. Morphological and protein expression changes in stenotic hVECs under oxidative stress conditions. (A) Immunofluorescent staining representing GSH (*green*) and β-actin filaments (*red*) arrangement in stenotic hVECs at steady state and after 4 h of treatment with DMSO or 2-AAPA 50 μM and 24 h of recovery. Cell nuclei were visualized with DAPI (*blue*). Scale bar: 50 μM. **(B)** Western blot representative images of stenotic hVECs after 4 h of 2-AAPA 50 μM treatment and 24 h of recovery. Antibodies against CD31, MMP2, TIMP2, and β-Actin were used. P-MMP2: pro-MMP2; C-MMP2: cleaved-MMP2. **(C–F)** Scatter plots with bar of Western blot relative quantification performed by ImageJ (CD31: Untreated $n = 11$; DMSO $n = 9$; 2-AAPA 50 μM $n = 11$; P-MMP2 Untreated $n = 8$; DMSO $n = 7$; 2-AAPA 50 μM $n = 8$; C-MMP2: Untreated $n = 8$; DMSO $n = 8$; 2-AAPA 50 μM $n = 8$; TIMP-2: Untreated $n = 8$; DMSO $n = 8$; 2-AAPA 50 μM $n = 8$). *t*-test: $^{***}p \le 0.001$; $^{*}p \le 0.05$.

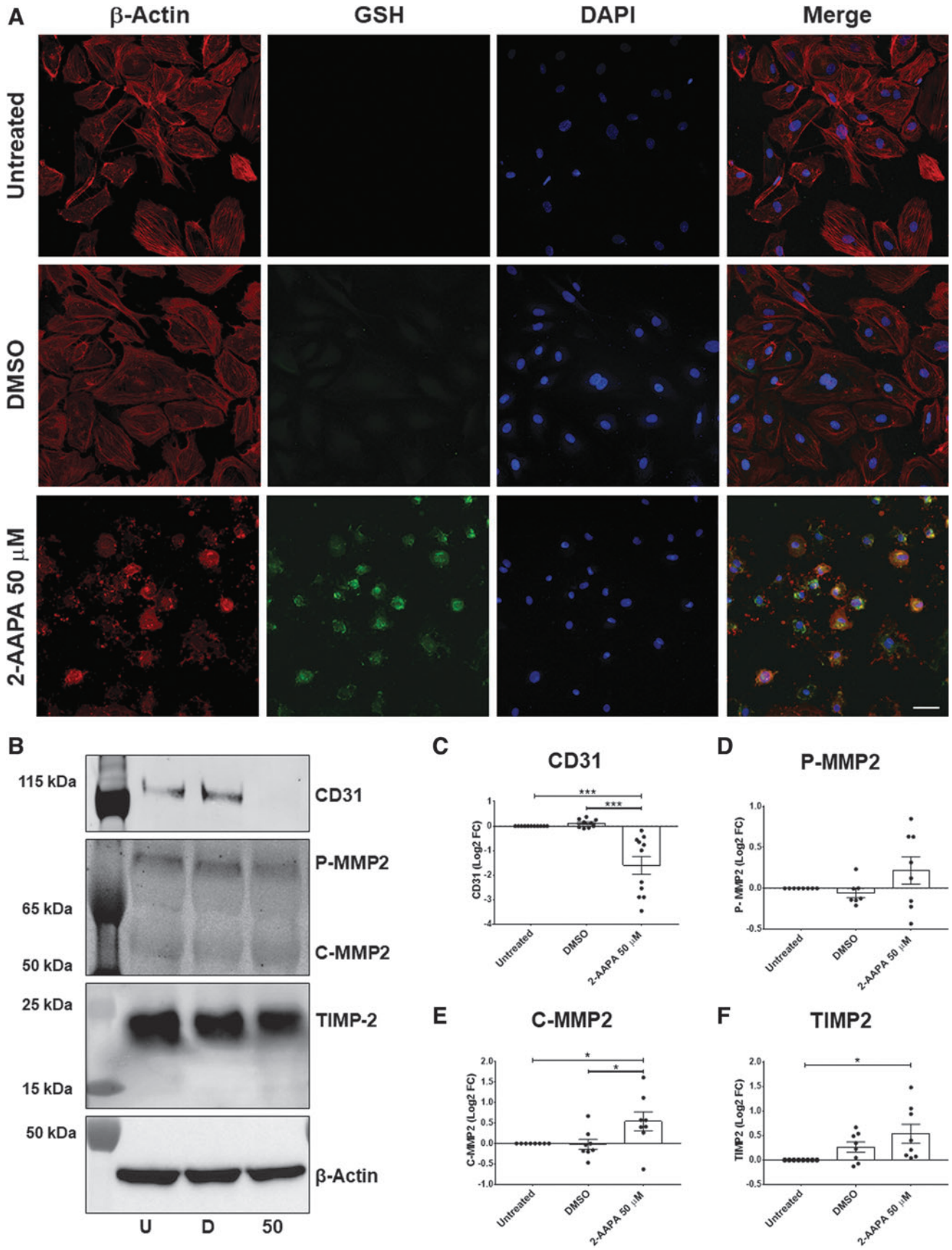
A
β-Actin
GSH
DAPI
Merge
Untreated
DMSO
2-AAPA 50 μM
B
115 kDa
CD31
P-MMP2
65 kDa
C-MMP2
50 kDa
25 kDa
TIMP-2
15 kDa
50 kDa
β-Actin
U
D
50
C
CD31
CD31 (Log2 FC)
D
P-MMP2
P- MMP2 (Log2 FC)
E
C-MMP2
C-MMP2 (Log2 FC)
F
TIMP2
TIMP2 (Log2 FC)
Untreated
DMSO
2-AAPA 50 μM

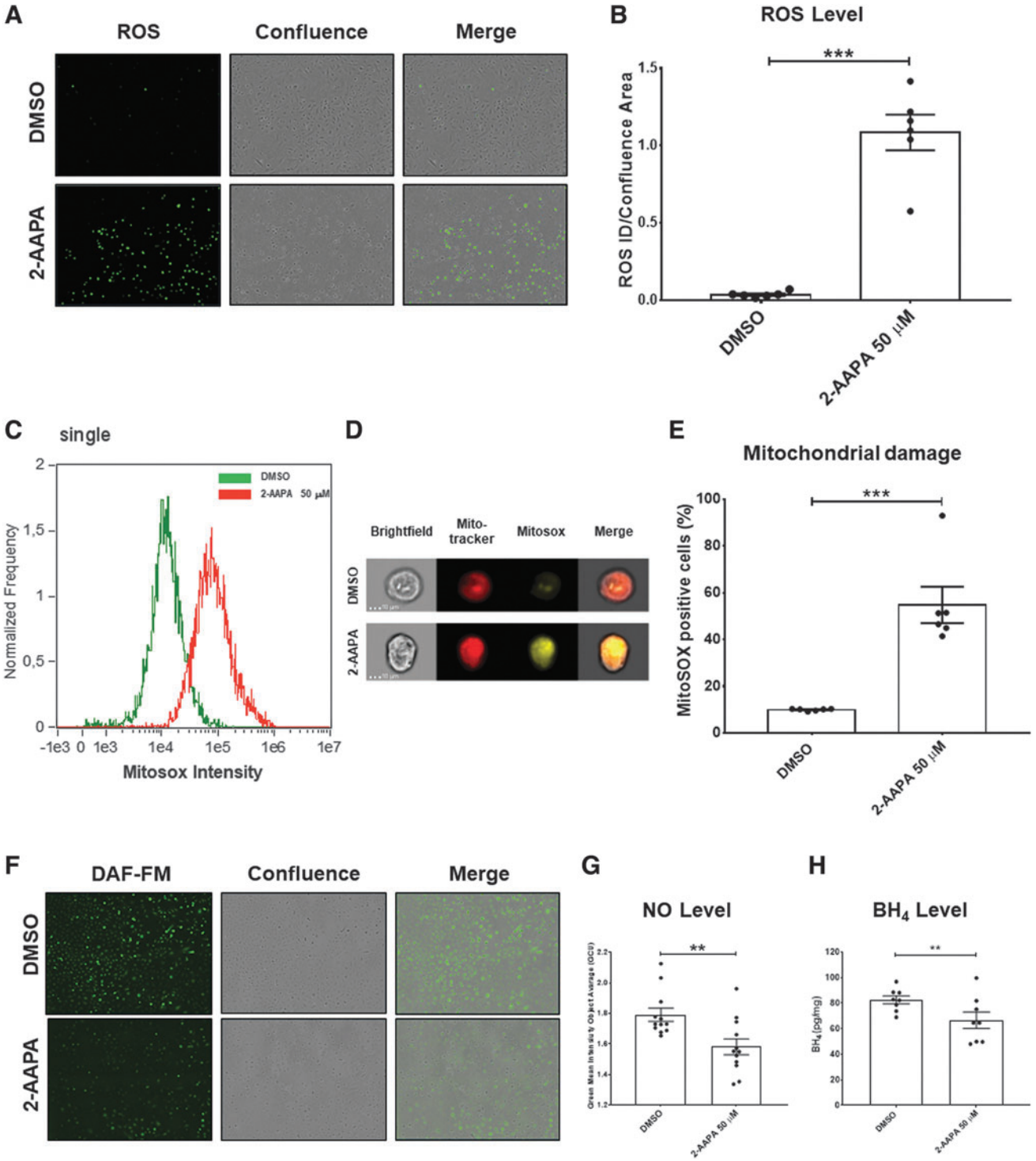

FIG. 6. ROS level, mitochondrial damage, and eNOS uncoupling in stenotic human endothelial cells under oxidative stress condition. (A) Immunofluorescence staining representing ROS (*green*) and phase-contrast images of stenotic hVECs subjected to DMSO (*upper panels*) and 2-AAPA 50 μM (*lower panels*) treatment (10×). **(B)** Scatter plot with bar of ROS level quantification ($n=6$). **(C, D)** Image flow cytometry analysis of mitochondrial damage (MitoTracker in *red* and Mitosox in *yellow*) in hVECs treated with DMSO and 2-AAPA 50 μM (40×). **(E)** Scatter plot with bar showing the percentage of Mitosox hVECs positive cells after 2-AAPA 50 μM treatment ($n=6$). **(F)** Immunofluorescence staining representing NO levels (DAF-FM in *green*) and phase-contrast images of hVECs subjected to DMSO (*upper panels*) and 2-AAPA 50 μM (*lower panels*) treatment (10×). **(G)** Scatter plot with bar of NO levels expressed as *green* mean intensity object average (GCU) ($n=12$). **(H)** Scatter plot with bar of BH_4 levels in hVECs treated with DMSO and 2-AAPA 50 μM ($n=8$). ***$p \leq 0.001$; **$p \leq 0.01$; *t*-test. eNOS, endothelial nitric oxide synthase.

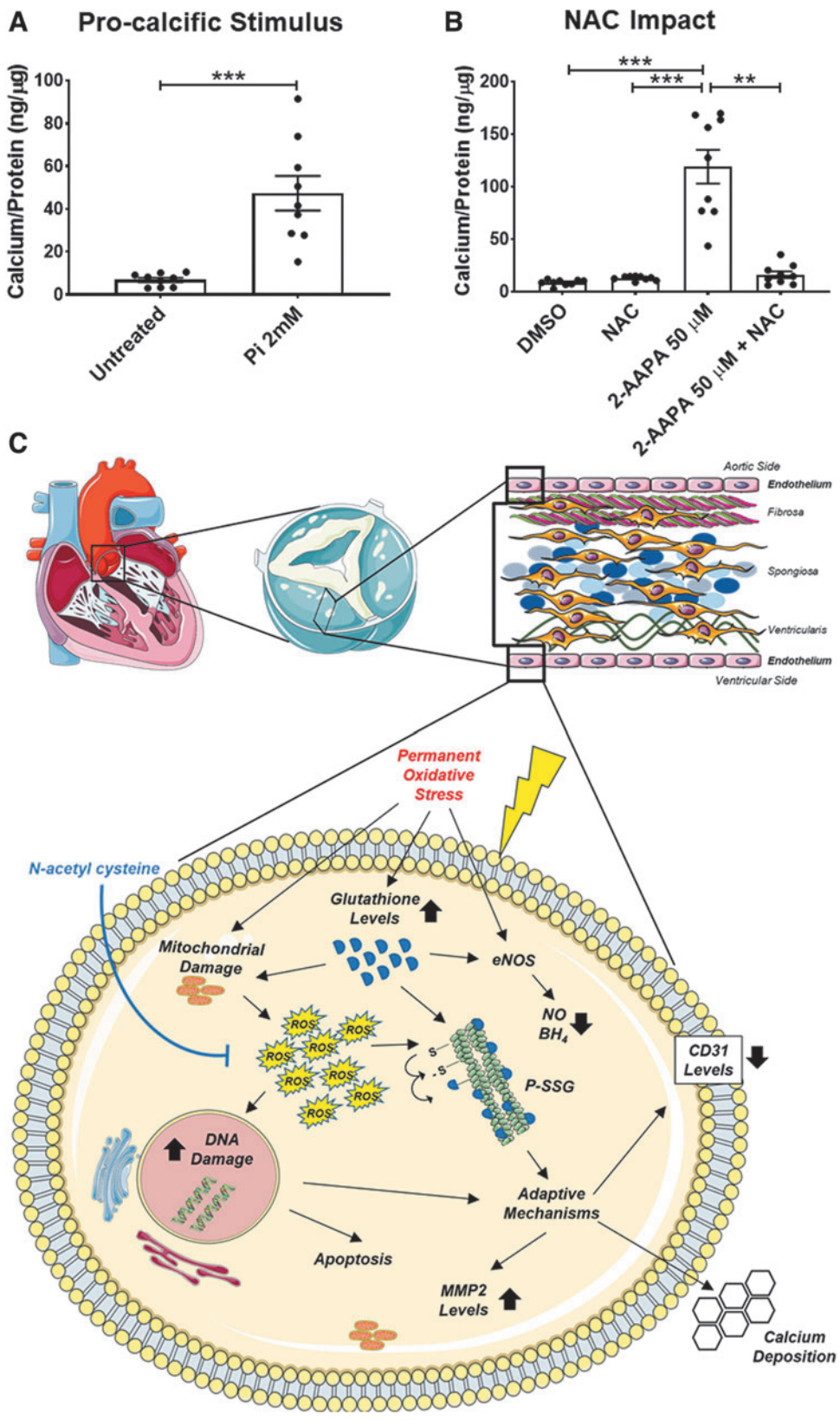

FIG. 7. Calcium deposition potential of human stenotic VECs. **(A)** Scatter plot with bar representing extracellular calcium quantification on hVEC treated with normal medium or 2 m*M* inorganic phosphate (Pi) for 7 days ($n=9$). **(B)** Scatter plot with bar showing calcium quantification on hVECs after 4 h of treatment and 7 days of recovery. Treatments: DMSO, NAC 2 m*M*, 2-AAPA 50 μM, or 2-AAPA 50 μM + NAC 2 m*M* ($n=9$). $^{***}p \leq 0.001$; $^{**}p \leq 0.01$; *t*-test. **(C)** Summary cartoon depicting oxidative stress and P-SSG involvement in VEC adaptive mechanisms leading to calcification.

from a sclerotic to a stenotic phenotype, a switch paralleled by a similar progressive increment in P-SSG deposition. Moreover, the present findings suggest that borne as a compensatory system to face an excessive oxidative burden, P-SSG favors the switch of hVECs from an innate endothelial phenotype to a damaged one, paving, in turn, the way to calcium deposition. Relevant from a translational perspective, our study unearths that the antioxidant compound, NAC, effectively prevents P-SSG in VECs and their subsequent calcification (Fig. 7c).

The AS, the end-stage phase of CAVS, is the third most common cardiovascular ailment after hypertension and coronary artery disease, being the most prevalent heart valve disorder in the western world (42, 57). The AS prevalence is about 3% in the 65 year-old population and older, increasing with advancing age (51): from 0.2% in the 50–59-year group to 9.8% in those aged 80–89 years (17). Despite severe AS being estimated to march up by 2.4-fold in the year 2040 and likely to escalate more than triple by 2060 (17), no current effective pharmacological treatment for preventing or arresting CAVS progression is available at the moment, therefore resting on surgical or transcatheter AVR as the sole available options nowadays. The CAVS remains a debilitating disease with a massive socioeconomic burden (7).

The CAVS is a complex, active progressive disease characterized by a cascade of cellular events that initially cause fibrotic thickening (*i.e.,* AVSc), followed by the extensive calcification of the aortic valve leaflets (*i.e.,* AS). This involution entails several tissue/cellular alterations, such as endothelial dysfunction, inflammatory cell recruitment, and VIC phenotypic switching in an osteoblast-like phenotype (40, 53). At least in part, these perturbations directly emanate from specific molecular processes, such as TGF-β signaling, bone morphogenetic protein signaling, wnt/β-catenin signaling, notch signaling, MMPs, and ROS (30, 53).

Our data add to this scenario a significant feature: Despite the upregulation of some non-enzymatic antioxidant systems, such as the glutathione one, ROS emission from human aortic leaflets continues to grow with time, marking the transition from a sclerotic to a stenotic phenotype. Until now, however, very few studies attempted to connect altered valve cell redox conditions to CAVS final stage (*i.e.,* AS) (22, 43). Nevertheless, in some instances, the strategy adopted to index ROS contribution was sub-optimal, as in the case of the use of dihydroethidium fluorescence to detect superoxide that is not so specific (37).

However, in other studies, ROS contribution was inferred by changes in the expression and activity of antioxidant enzymes such as superoxide dismutase and catalase (11, 22, 43). Paradoxically, no studies have delved into the glutathione system yet, that is, the primary non-enzymatic antioxidant system and reducing equivalents' providers in the cell (5, 23, 61). GSH is present in millimolar concentrations in eukaryotic cells' cytosol (64) and, under normal conditions, the GSH/GSSG ratio ranges from 30:1 to 100:1 (35).

During high ROS emission conditions, cells put up reversible S-glutathionylation to guard highly reactive cysteine residues from permanent oxidative modifications (55). Here, for the first time, we performed a direct GSH/GSSG ratio assessment in human endothelial cells isolated from aortic valves at different stages of the disease, employing a state-of-the-art approach, such as LC-MS/MS, previously mentioned to be developed in our lab (68).

Our studies in human valves reveal a progressive GSH/GSSG ratio increment during CAVS disease, suggesting adaptive efforts to face the enduring oxidizing conditions occurring in stenotic valve cells. Further, we proved the centrality of persistently elevated ROS emission in CAVS involution toward a stenotic phenotype by using an *in vitro* approach. In this model, both induction and scavenging of P-SSG *via* de-glutathionylation are still at play.

When removed from the *in situ* highly oxidizing conditions occurring in the diseased human valve tissues and placed in a culture system where de-glutathionylation can intervene, human stenotic VECs showcase P-SSG levels that are superimposable to those found in control valves. These data suggest that *in situ* persistent P-SSG levels in human stenotic cells act as a ''redoxstat''; simultaneously, they testify the persistence of elevated ROS emission experienced by the valve tissue. In the end, P-SSG can ultimately serve to counter some ROS-mediated effects in valve cells.

For instance, in the present case, it may explain why human stenotic cells display increased viability compared with both controls and sclerotic cells. Notwithstanding, persistently elevated ROS and P-SSG levels in stenotic cells—the latter likely due to a reduced de-glutathionylation ability—seemingly factor in the morphological/functional switch of the endothelial phenotype. Ultimately, these alterations predispose human stenotic cells to calcium deposition. In aid of this contention come data evaluating the mitochondrial damage and eNOS dysfunction. Indeed, during persistent oxidizing conditions, many mitochondrial proteins are S-glutathionylated as an attempt to protect, however causing ROS leakage at the end (69).

Further, under oxidative stress conditions, when P-SSG arises, a process known as eNOS uncoupling occurs (18). When eNOS uncouples instead of producing $NO^{\cdot}$ it makes $O_2^{\bullet-}$ (14), a process that can be monitored by BH_4 reduction (25) as observed in our experiments. Finally, the loss on CD31, a classic endothelial marker, and the increment in MMP2 expression could also highlight a possible consequence of an endothelial-to-mesenchymal transition (73). At the same time, here, we report the upregulation of MMP2, a protein involved in matrix remodeling that is overexpressed whenever cells acquire invasive properties, thus the possibility of migrating toward the aortic valve's inner layers (39).

Present studies with NAC further corroborate the concept that unremitted ROS emission from valve cells favors CAVS progression toward stenosis. This exogenous thiol compound is an acetaminophen poisoning antidote (33), ROS scavenger (2), and reduced glutathione precursor (72). However, the passage of NAC through the plasma membrane is problematic in that its carboxyl group loses its proton at physiological pH, making the compound negatively charged (4). In our proof-of-concept experiments, we use a high concentration of NAC (2 m*M*) to overpass this limitation.

The NAC impact has been tested in a plethora of cardiovascular disease models, highlighting its effectiveness in countering oxidative stress; attenuating fibrosis (58), ischemia-reperfusion injury (6), and apoptosis (12). The NAC reduces systemic and myocardial oxidative stress in CAVS pathophysiology by restoring total myocardial glutathione while attenuating myocardial fibrosis in an AS rat model (58). It can also halt fibrosis and AS progression in mice with the genetic deletion of the low-density lipoprotein receptor (LDLR), by reducing the shear-dependent activation of TGF- β1 potentially *via* a thiol-disulfide exchange mechanism and not ROS (65).

However, despite these models being flawed by several limitations, including the different anatomical structures of the aortic valve of rodents *versus* humans and the need to introduce dietary regimens or genetic interventions to induce

valve calcification (60), they indicate that NAC could potentially be a treatment for AS. Further, our evidence showing that NAC prevents the modification of cysteines in the VECs, their S-glutathionylation, and calcification attests to the relevance of also countering ROS progressive accumulation.

Several clinical trials tested NAC effectiveness in cardiovascular diseases, as both a short- and long-term treatment (9, 15, 16, 31, 34, 67). Tepel *et al.*, for instance, showed NAC-induced protection toward composite cardiovascular endpoints, under pathological conditions such as fatal and nonfatal myocardial infarction, cardiovascular disease death, need for coronary angioplasty, coronary bypass surgery, coronary bypass surgery, and ischemic stroke, or peripheral vascular disease with amputation (67).

Interestingly, NAC attenuates *in vivo* oxidation of injected human LDL, eventually reducing atherosclerotic plaque formation (16). Notably, oxidized LDL fuel CAVS progression through an osteogenic program (46). Also worth mentioning is that NAC, at intermediate dosages (1200 mg daily) and given chronically (12–24 months), shows no major side effects (9, 67). Besides its antioxidant properties, NAC can decrease the gelatinolytic activity of MMPs, with effects likely due to NAC's ability to scavenge ROS or direct interaction with gelatinases (8).

Thus, there is ample theoretical room for thinking that NAC, perhaps as an adjuvant, could contribute to preserving the valve endothelium, preventing its progression toward a stenotic phenotype. However, this possibility remains to be tested. Consequently, NAC has been used here just as a proof of principle.

This study has some limitations; thus, aspects warrant future, more in-depth investigation. First, we evaluated P-SSG with a dot blot and Western blot approach, where the latter revealed a single sharp band at the molecular weight of β-actin, as previously described by our group (68). In so doing, we could not detect P-SSG on other proteins, possibly due to the antibody's sensitivity. However, our data align with the literature where P-SSG causes structural and functional proteins' modifications (27, 28).

Besides, we did not delve into the endothelium/interstitium crosstalk. Indeed, we aimed at unveiling endothelial cell contribution (and their transformation) to CAVS progression from a sclerotic to a stenotic phenotype for the present study. In addition, we performed short-term *in vitro* cell culture experiments, and thus, they might not entirely reflect the chronic pathophysiology of AS, which takes many years to develop. However, it is interesting to note that we used endothelial cells isolated from aortic leaflets at different stages of the pathology.

They seem to retain peculiar characteristics at a certain degree, suggesting adaptive efforts to face the enduring oxidizing conditions. Finally, 2-AAPA treatment has been linked to cellular senescence (41) and, in our *in vitro* system, we noticed an increment in the phosphorylation of the histone H2AX, the second most common senescence marker. However, we checked the levels of cyclin-dependent kinase inhibitor 1A (p21/Cip1), another well-known marker of senescence, after 2-AAPA treatment. No significant regulation was found. In essence, we are not naively saying that the present findings exhaust all possible mechanistic explanations in this sense.

Conclusion

Our study demonstrates that unremitted ROS emission from endothelial cells, along with a P-SSG build-up, occurs and accounts, at least in part, for the morphological/functional changes occurring in the human aortic valves when they switch from sclerotic to stenotic, increasing the chance of calcification. Our *in vitro* data suggest that it is possible to de-activate this mechanism, leveraging on endogenous signaling or exogenous compounds that are able to blunt ROS emission and counter MMP expression/activity, as suggested herein by the use of NAC.

In our view, two main complementary avenues should be pursued to arrest aortic valve disease progression. First, blunting ROS emission to reduce the need for P-SSG; then, preserving the endothelium integrity/function. In the end, both measures will conjure up to prevent the onset of maladaptive processes, ultimately paving the way to calcium deposition and thus stenosis.

Materials and Methods

Patient enrollment and the study protocol

We prospectively obtained human aortic valve leaflets from patients undergoing AVR at Centro Cardiologico Monzino IRCCS (CCM). The study was approved by the Institutional Review Board and by the Ethical Committee of CCM according to the principles outlined in the Declaration of Helsinki (1964). We asked each enlisted patient to sign informed consent to use the removed aortic valve leaflets. In particular, we enrolled patients with tricuspid aortic valves intended for AVR surgery without sclerosis (control; $n = 18$), with sclerosis (AVSc; $n = 23$), and with severe stenosis (AS; $n = 25$).

In detail, we obtained aortic valve leaflets from patients requiring AVR and divided into: (i) controls, patients who underwent AVR due to aortic valve insufficiency with normal aortic valve leaflet structure; (ii) sclerosis, patients who underwent AVR due to aortic valve insufficiency with AVSc; and (iii) stenosis, patients who underwent AVR due to severe AS. Aortic valve insufficiency was categorized as: no (0), mild (1), moderate (2), and severe (3) regurgitation during echocardiography procedure (7).

The presence of AVSc was recognized as non-uniform thickening with or without spotty calcified areas of the aortic valve leaflets without a significant transvalvular gradient (maximum aortic velocity <2.5 m/s), as described by Otto *et al.* (47). The presence of AVSc was ascertained by an expert echocardiographer and an experienced surgeon who shed light on borderline cases. Severe AS patients were defined according to current guidelines (*i.e.,* aortic jet velocity >4.0 m/s, mean gradient ≥40 mmHg, and aortic valve area <1 cm^2) (7).

We used the following inclusion criteria: (i) elective and isolated surgical procedure; (ii) older than 18 years of age; (iii) ejection fraction >30%; and (iv) normal sinus rhythm. We adopted the following exclusion criteria: Bicuspid aortic valve morphology, previous cardiac surgery, rheumatic heart disease, endocarditis, active malignancy, chronic liver or kidney diseases, calcium regulation disorders (hyperparathyroidism, hyperthyroidism, and hypothyroidism), and chronic or acute inflammatory states (sepsis, autoimmune disease, and inflammatory bowel disease) were considered exclusion criteria.

The demographic and clinical features of enrolled patients are viewable in Supplementary Table S1. After the surgical procedure, the aortic valve leaflets removed were collected and processed within 30 min. In detail, aortic leaflets were snap-frozen, paraffine-embedded, or used for ''cells'' isolation.

EPR analysis

As previously described, ROS measurements were conducted by using EPR spectroscopy (13, 38). Flash-frozen human aortic valve tissue ($\sim$20 mg) was homogenized by using a hand-held homogenizer in phosphate-buffered saline (PBS; Lonza Group, Basilea, Swiss, Cod: LOBE17513F, pH 7.4) containing protease inhibitor cocktail (cOmplete™, Mini, EDTA-free Protease Inhibitor Cocktail; MilliporeSigma, Burlington, MA, Cod: # 11836170001, pH 7.0) and 0.1 m*M* of the metal chelator diethylenetriaminepentaacetic acid (DTPA; Sigma-Aldrich, St. Louis, MO, Cod: # 284025), at pH 7.4. Non-soluble fractions were removed by centrifugation at 15,000 *g* for 10 min (4°C).

The homogenates were kept on ice and analyzed immediately. Stock solutions of the spin probe 1-hydroxy-3-methoxycarbonyl-2,2,5,5-tetramethyl-pyrrolidine hydrochloride (CMH; Enzo Life Sciences, Farmingdale, NY, Cod: # ALX-430-117-M050) were prepared daily in nitrogen-purged 0.9% (w/v) NaCl (Hospira, Inc., Lake Forest, IL, Cod: #0409196602), 25 g/L Chelex 100 (Bio-Rad, Hercules, CA, Cod: # 1421253), and 0.1 m*M* DTPA, and they were kept on ice.

The samples were treated with 1 m*M* CMH at 37°C for 2 min, transferred to 50-μL glass capillary tubes, and analyzed immediately on a Bruker E-Scan (Billerica, MA) EPR spectrometer at room temperature. Spectrometer settings were as follows: sweep width, 100 G; microwave frequency, 9.75 GHz; modulation amplitude, 1 G; conversion time, 5.12 ms; receiver gain, 2×10^3; and number of scans, 16. In all cases, the samples were in the linear response region. The EPR signal intensities were assessed by measuring the EPR signal peak-to-peak amplitude. The reported ROS levels represent EPR signal intensities normalized to the tissue ''homogenates'' protein concentrations as the Pierce BCA protein assay kit determined.

Immunohistochemistry

Aortic valve leaflets for histological analysis were washed three times in PBS 1×(Lonza Group, Cod: LOBE17513F, pH 7.4); they were fixed in 4% formalin (Sigma-Aldrich; Cod: HT501128-4L, pH 6.9–7), dehydrated, included in paraffin (Vwr International Pbi S.R.L., Milan, Italy, Cod: T8234701-5), and cut into 5–7 μm slides. Before staining, slides were rehydrated, incubated in antigen retrieval solution (Target Retrieval Solution Citrate [pH 6], Dako Cytomation, Glostrup, Denmark, Cod: S169984-2) at 98°C for 20 min, and then cooled at room temperature for 20 min.

Slides were treated with 3% H_2O_2 to block endogenous peroxidase and then washed three times with 1×PBS with 0.1% TritonX (Merk Life Science S.R.L., Milan, Italy, Cod: X100-100ML) (PBST). Blocking solution [PBST and 5% BSA (Sigma-Aldrich; Cod: 05482-25G)] was added and kept for 45 min at room temperature. Slides were incubated with primary mouse monoclonal anti-GR at 4°C overnight. Slides were washed three times with PBST and incubated with biotinylated anti-mouse secondary antibody for 60 min at room temperature.

Slides were washed three times, and the ABC complex was added and incubated for 30 min at room temperature. Slides were washed three times, and ImmPACT DAB Peroxidase (HRP) Substrate (Vector Laboratories, Burlingame, CA; PK6100) was added and left to react for 25 s. Slides were immediately rinsed in distilled H_2O and then incubated for 10 s with hematoxylin (Agilent Technologies Italia Spa, Cernusco sul Naviglio, Italy).

Slides were dehydrated and mounted with EUKITT (Bio Optica, Milano, Italy, Cod: 09-00502), and images were taken with AxioScope (Carl Zeiss). The quantification of GR immunohistochemistry has been performed by implementing the ImageJ v1.50i software (NIH, Bethesda, MD) with the IHC Toolbox plugin. The automated color detection, which allows the generation of deconvoluted images, has been performed with the default model H-DAB for brown color detection. The integrated pixel density has been calculated on binary panoramic images and normalized with the total area of the section (pixel^2).

Aortic valve endothelial "cells" isolation

The porcine aortic valves were obtained from healthy pig hearts intended for slaughter for food purposes. Isolation of endothelial valve cells from pigs (pVEC) and human (hVEC) patients enrolled was performed by using an implemented method previously described by our group (54, 62). Concisely, after removal, the aortic valve leaflets were incubated for 20 min at 37°C in a solution composed of 2 mg/mL type II collagenase (Worthington Biochemical Corp., Lakewood, NJ, Cod: CLS-2) and Advanced DMEM (AdDMEM; Thermo Fisher Scientific, Waltham, MA, Cod: 12491015) enriched with 10% FBS (Thermo Fisher Scientific; Cod: 26140079), 1% Penicillin-Streptomicin (Thermo Fisher Scientific; Cod: 15140122) solution.

After incubation, the loose endothelial layer was removed by pipetting the previously described solution onto the valve surface. The resulting cells were washed with PBS 1×(Lonza Group, Cod: LOBE17513F, pH 7.4) and isolated by using Dynabeads® (CD31; Life Technologies, Carlsbad, CA, Cod: 1155D) conjugated with an endothelial marker, platelet endothelial cell adhesion molecule. Then, VECs were cultured in supplemented Medium 200 (M200; Thermo Fisher Scientific, Cod: M200500) on a 0.1% gelatin-coated (Sigma-Aldrich; Cod:G1890-100G) tissue culture plate (Corning® Costar®; New York, NY, Cod:CLS430167). All experiments were performed on cultured cells between the second and fifth passages.

In vitro *model of oxidative stress and P-SSG*

In vitro model of S-glutathionylation was prepared by transposing and implementing a method previously described by Valerio *et al.* (68). The GR and thioredoxin reductase systems were blocked (19), in pVEC, by using a specific compound known as 2-acetylamino-3-[4-(2-acetylamino-2-carboxyethylsulfanylthiocarbonylamino)phenylthiocarbamoylsulfanyl]propionic acid (2-AAPA; Sigma-Aldrich) titrating the dose as follows: 12.5, 25, 50, 75, and 100 μ*M*.

This compound was used as an internal control since 2-AAPA was dissolved in dimethyl sulfoxide (DMSO; Sigma-Aldrich, Cod: D8418-100ML).

The pVECs were treated with 2-AAPA in complete M200 medium for 4 h. After 24 h of recovery, protein levels and ROS production were evaluated. We found that the minimum effective dose of 2-AAPA in pVECs was 50 μM; therefore, we treated hVEC with this drug concentration and performed assays such as protein level GSH/GSSG, MTT, and apoptosis assessment by using this 2-AAPA dosage.

During the calcification assays, we challenged hVECs with different stimuli: (i) a pro-calcifying one, consisting of a standard medium supplemented with 2 mM inorganic phosphate (Pi Buffer: Sodium phosphate dibasic, [Sigma-Aldrich; Cod: 106586] titrated with Sodium phosphate monobasic [Sigma-Aldrich; 106586]) administered every 2 days while changing the medium every time; (ii) a pro-oxidative challenge by providing 2-AAPA (50 μM for 4 h) and changing the media every 2 days; and (iii) an antioxidant treatment encompassing 1 h of pretreatment with 2 mM N-acetyl-L-cysteine (NAC; Santa Cruz, CA, Cod: sc-202232A), followed by for 4 h with 2-AAPA (50 μM) + NAC (2 mM) and NAC (2 mM) was administered every 2 days while changing the medium. Each assay lasted 1 week.

Glutathione dosages

The two different forms of glutathione, reduced (GSH) and oxidized (GSSG), were detected in cell extracts obtained after treatment by the LC-MS/MS method, as previously described (63, 68). In detail, standard solutions were prepared daily by diluting the stock solutions of γ-L-glutamyl-L-cysteinyl-glycine (GSH; Sigma-Aldrich, Cod: G4251), and γ-L-glutamyl-L-cysteinyl-glycine disulfide (GSSG, product number: G4376; Sigma-Aldrich) with 0.1% formic acid.

Chromatographic separation was conducted on a Luna PFP analytical column (100 × 2.0 mm, 3 μm; Phenomenex, Torrance, CA, 00D-4447B0) under isocratic conditions with 99% mobile phase A (ammonium formate 0.75 mM adjusted to pH 3.5 with formic acid) and 1% mobile phase B (methanol; Merk Life Science S.R.L., Cod: 322415), at a flow rate of 200 μL/min and a column temperature of 35°C. The total run time per sample was 10 min, and all injection volumes were 10 μL. Mass spectrometric analysis was performed by using a TSQ Quantum Access (Thermo Fisher Scientific) triple quadrupole mass spectrometer coupled with electrospray ionization operated in multiple reaction monitoring (MRM) in positive mode.

The MRM for GSH (m/z 308.1 → m/z 76.2 + 84.2 + 161.9) and GSSG (m/z 613.2 → m/z 230.5 + 234.6 + 354.8) were performed with collision energy optimized for each compound. The operating conditions for the MS analysis were as follows: spray voltage, 2500 V; capillary temperature and voltage, 280°C and 35 V, respectively; sheat gas and auxiliary gas flow, 30 and 5 AU, respectively; and tube lens offset, 84 V for GSH and 115 V for GSSG. The mass spectrometer was employed in the MS/MS mode by using argon as collision gas.

Data acquisition and analysis were performed with Xcalibur® software, version 2.0 (Thermo Fisher). After comparing calibration curves, data were obtained by using GSH (Sigma-Aldrich; GA251) and GSSG (Sigma-Aldrich; GA376) pure standard solutions. The intra- and inter-CVs (%) obtained with standard samples were <5% for both the analytes. The detection limits were 0.031 μM for GSH and 0.008 μM for GSSG.

Dot blot and Western blot analyses

Human aortic valve tissue and VECs isolated from human and porcine specimens were lysed in RIPA Buffer 1 × (Igepal 1% (Sigma-Aldrich; Cod: I8895-50ML), sodium dodecyl sulfate (SDS; Sigma-Aldrich, Cod: L3771-25G) 0.1%, 50 mM Tris-HCl (Sigma-Aldrich; Cod: T446-100G), 150 mM NaCl, 0.5% sodium deoxycholate (Sigma-Aldrich; Cod: D6750), and 1 mM EDTA (Sigma-Aldrich; Cod: E4884, pH 7.5), with protease and phosphatase inhibitors (Thermo Fisher Scientific; Cod: 88665 and 88667, respectively).

All cell samples were pre-treated with 10 mM N-ethylmaleimide (NEM; Thermo Fisher Scientific, Cod: 23030) for 5 min in a complete medium before lysis to alkylate the free thiols and thus avoid the formation of artifacts during protein glutathionylation detection. After quantification with BCA Protein Assay Kit (Thermo Fisher Scientific; Cod: 23225), total protein extracts from tissues were subjected to dot Blot, whereas total protein extracts from cells were subjected to SDS-page under non-reducing conditions for GSH detection and under reducing conditions for CD31 (Cell Signaling, Danvers, MA; Cod: #3528), MMP2 (Novus Biologicals, Minneapolis, MN; Cod: NB200-193SS), TIMP2 (Cell Signaling; Cod: #5738) detection.

All Western blot experiments were carried out by using gel with the gradient percentage of polyacrylamide, from 4% to 12% (Bolt™ 4 to 12%, Bis-Tris, 1.0 mm, Mini Protein Gel, 10-well; Thermo Fisher Scientific, Cod: NW04120BOX). Runs were performed with the running buffer MOPS SDS 1 × (Thermo Fisher Scientific; Cod: NP0001, pH 7.7) at constant 200V. Then, the proteins were transferred onto a nitrocellulose membrane, using the iBlot Transfer Stacks (Thermo Fisher Scientific; Cod: IB301002) with iBlot1 Gel Transfer Device (Thermo Fisher Scientific).

For blocking non-specific sites, the membranes were treated for 30 min at room temperature in 5% skim milk (Sigma-Aldrich; Cod: 70166-500G), dissolved in Wash Buffer (Tris Buffer Sulfate 1 ×, 0.1% Tween 20; Sigma-Aldrich, Cod: T4661-100G and Pi379 respectively, pH 7.6), and finally incubated O/N at 4°C, slowly stirring, with the appropriate primary antibody.

We used Ponceau (Sigma-Aldrich; Cod: P3504-10G) and β-Actin (Cell Signaling; Cod: #4970) as loading controls, respectively, for Dot blot and Western blot; GSH (Santa Cruz, CA, Cod: sc-52399), yH2AX (Cell Signaling; Cod: #9718S), CD31 (Cell Signaling; Cod: #3528), MMP2 (Novus Biologicals; Cod: NB200-193SS), and TIMP2 (Cell Signaling; Cod: #5738) to detect target protein. Then, Dot blot and Western blot membranes were washed to remove any excess of primary antibody and incubated, respectively, with peroxidase-conjugated secondary antibody (Peroxidase-AffiniPure Sheep Anti-Mouse IgG, F(ab')2Fragmnwnt Specific; Jackson ImmunoReserch Laboratories, Inc., Baltimore Pike, PA, Cod: 515-035-072) and IRDye conjugated secondary antibody (LI-COR Biosciences, Lincoln, NE, IRDye 800CW Donkey anti-Mouse Cod: 925-32212 and IRDye 680RD Donkey anti-Rabbit Cod: 925-68073) for 1h in the first case and 20 min in the second case at room temperature.

Finally, the membranes were washed to remove any excess secondary antibody, and images were acquired by using the Alliance Mini 2M (UVITec, Cambridge, United Kingdom) and the Odyssey Infrared Imaging System (LI-COR Biosciences). Densitometry analysis was performed by using the software ImageJ (Version 1.48v – National Institute of Health).

Tetrahydrobiopterin ELISA kit

Protein cell lysates, previously prepared after 4 h of 2-AAPA (Sigma-Aldrich; Cod: A4111) 50 μM treatment and 24 h of recovery, were loaded into the microplate provided in the kit pre-coated with BH_4 (Tetrahydrobiopterin ELISA Kit [Colorimetric] [Novus Biological, a Biotecne Brand, MN, Cod: NBP2-74983]). The ELISA assay was carried out in accordance with manufacturing instructions. Finally, the enzyme-substrate reaction was measured spectrophotometrically at a wavelength of 450 nm by using the microplate reader (TECAN pro infinite M200). The concentration of BH_4 in the sample was then determined by comparing the OD of the samples with the standard curve. The pg/mL of BH_4 found were normalized to the mg/mL of protein measured with BCA Kit.

Intracellular ROS and NO detection

The pVECs were grown to sub-confluency in 60 mm plates (Corning® Costar®; 430166) coated with 0.1% of gelatin (Sigma-Aldrich; Cod: G1890-100G) in a complete M200 medium (M200; Thermo Fisher Scientific, Cod: M200500). Similarly, hVECs were seeded in 96-well plates coated with 0.1% gelatin. After 4 h of 2-AAPA (Sigma-Aldrich; Cod: A4111) 50 μM treatment and 24 h of recovery, ROS detection was performed by CellROX® green Assay Kit (Thermo Fisher Scientific; Cod: C10492), executed following the manufacturer's instruction. The staining for pVECs was analyzed by ImageStream X imaging flow cytometer (ImageStream X Mark II, Amnis).

The analysis was performed by using the IDEAS 6.2 software. In parallel, in hVECs, using a system of automated live-cell imaging (IncuCyte S3, Sartorius, Gottingen, Germany), we assessed ROS, by CellROX green Assay Kit, and nitric oxide (NO) levels, by 4-Amino-5-Methylamino-2',7'-Difluorofluorescein Diacetate (DAF-FM; Thermo Fisher Scientific, Cod: D23841).

MTT assay

hVECs and pVECs were seeded in 96-well plates coated with 0.1% gelatin (Sigma-Aldrich; Cod: G1890-100G) in a complete M200 (Thermo Fisher Scientific; Cod: M200500) growing medium. After cell adhesion, a starvation protocol was carried out overnight in M200 without FBS. After 1 day, starvation was terminated, and the cells were treated with 2-AAPA (Sigma-Aldrich; Cod: A4111) in M200 with 0.5% FBS. After the 4 h of treatment and 24 h of recovery, the medium was removed, and the 3-(4, 5-dimethyl thiazolyl-2)-2,5-diphenyltetrazolium bromide (MTT; Sigma-Aldrich, Cod: M2128) solution (0.5 mg/mL) was added into each well and incubated at 37°C, 5% CO_2 for 4 h.

After incubation, the MTT solution was discarded, and DMSO (Sigma-Aldrich; Cod: D8418-100ML) was added to each well and incubated for 10 min. Finally, the corresponding absorbance was measured by using the microplate reader (TECAN pro infinite M200) at a dual wavelength of 590 and 620 nm (reference).

Flow cytometry, apoptosis protein profiling, and mitochondrial damage

Annexin V (Thermo Fisher Scientific; Cod: V13241), a standard marker of apoptotic cells, was used to measure apoptosis levels after 2-AAPA treatments. Annexin V assay was performed on hVECs by using ImageStream X imaging flow cytometer (ImageStream X Mark II, Amnis). The hVECs were treated for 4 h with 2-AAPA 50 μM (Sigma-Aldrich; Cod: A4111), and afterward, they were subjected to 24 h of recovery in M200 (Thermo Fisher Scientific, Cod: M200500). Subsequently, cells were detached by an enzymatic method that was able to prevent damage to cell plasma membranes (TripLE™ Select Enzyme (1×) no phenol red (Thermo Fisher Scientific; Cod: 12563029), re-suspended in 100 μL of FACS buffer (PBS 1×; Lonza Group, Cod: LOBE17513F pH 7.4) supplemented with 0.1% BSA (Sigma-Aldrich, Cod: 05482-25G) and 5 mM Ethylenediaminetetraacetic acid disodium salt dihydrate (EDTA; Sigma-Aldrich, Cod: E4884)), and they were incubated in the dark for 15 min with the antibody Annexin V conjugated with Alexa Fluor488.

After incubation and washing with the FACS buffer, the cells were centrifuged for 10 min at 400 g to remove the unbound antibody eventually. Finally, cells were re-suspended in 100 μL of FACS buffer and after adding Propidium Iodide (Thermo Fisher Scientific; Cod: BMS500PI) analyzed at cytofluorimeter. The same procedure was performed for detecting mitochondrial localization and their superoxide production.

Particularly, after detachment, when re-suspended in 100 μL of FACS buffer, cells were incubated with Mito-Traker (a fluorescent dye that stains mitochondria in live cells and it is used for mitochondrial localization [Thermo Fisher Scientific; Cod: M22426]) and MitoSox (a reagent that permeates live cells and is rapidly oxidized by superoxide but not by other ROS or reactive nitrogen species [Thermo Fisher Scientific; Cod: M36008]) for 30 min at 37°C. The hVECs were gated on a side scatter-forward scatter dot plot to eliminate cell debris, and a total of 20,000 events in the hVECs gated area were acquired. Acquisition analysis was performed, thanks to the Kaluza software (Beckman Coulter, Brea, CA) and IDEAS 6.2 software (Luminex, Austin, TX).

For protein profiling, we used arrays provided by Human Apoptosis Array Kit (R&D systems, Minneapolis, MN; Cod: ARY009). We spotted total protein extract from stenotic cells treated with DMSO (Sigma-Aldrich; Cod: D8418-100ML) and 2-AAPA 50 μM and performed the procedure according to the manufacturer's instructions. The images were acquired by using the Alliance Mini 2M (UVITec), and densitometry analysis was performed by using the software ImageJ (Version 1.48v – National Institute of Health).

Immunofluorescence

The hVECs were seeded in 15 μM-Slide eight-well (Ibidi, Gräfelfing, Germany, Cod:80826) plates coated with 0.1%

gelatin (Sigma-Aldrich; Cod: G1890-100G) in a complete M200 (Thermo Fisher Scientific, Cod: M200500) growing medium. After the 4 h of treatment with 2-AAPA 50 μM (Sigma-Aldrich; Cod: A4111) and 24 h of recovery, the medium was removed, and the cells were fixed in 4% formalin (Sigma-Aldrich; Cod: HT501128-4L, pH 6.9–7) for 15 min.

After two washes with PBS 1×(Lonza Group, Cod: LOBE17513F, pH 7.4), cells were incubated for 10 min with methanol (kept at −20°C) to ensure permeabilization. Two washes with PBS 1×were carried out to remove excess methanol (Merk Life Science S.R.L.; Cod: 322415), and immediately afterward, the solution to block non-specific sites comprising 5% BSA (Sigma-Aldrich; Cod: 05482-25G), 0.5% donkey serum (Sigma-Aldrich; Cod: D9663), and 0.2% tritonX100 (Merk Life Science S.R.L.; Cod: X100-100ML) was added to the wells and incubated for 30 min at room temperature.

After two washes in PBS 1×, cells were incubated O/N in blocking solution with primary antibody against GSH (Santa Cruz, CA, Cod: sc-52399) and β-Actin (Cell Signaling; Cod: #4970). After two washes with PBS 1×, the cells were incubated with anti-mouse Alexa Fluor 488 secondary antibody (Abcam, Cambridge, United Kingdom, Cod: ab150113) for detection of GSH and anti-Rabbit Alexa Fluor 647 (Abcam; Cod: ab150075) for β-Actin detection. A drop of Vectashield Mounting Medium with Dapi (D.b.a Italia S.r.l., Milan, Italy, Cod: H-1200-10) was used to color the nuclei blue. The images were taken with a confocal microscope (Carl Zeiss).

Calcium deposition quantification

After removing the culture media, extracellular calcium crystals were dissolved under gentle agitation with 0.6 *M* hydrochloric acid (HCl; Sigma-Aldrich, Cod: 320331) for 5 h. Subsequently, HCl samples were recovered and stored at +4°C; meanwhile, the layer of cells present in each well was treated with 0.1 *M* sodium hydroxide (NaOH; Sigma-Aldrich, Cod: 30620) and 0.1% SDS (Sigma-Aldrich, Cod: L3771-25G) to ensure cellular lysis necessary for total protein quantification. Extracellular calcium quantification was performed by using a calcium colorimetric assay kit (BioVision, Milpitas, CA, Cod: K380) following the manufacturing company's protocol. The absorbance was read off at the Infinite® 200pro (TECAN) spectrophotometer.

Statistical analysis

Data analysis was performed by using Graph Pad Prism Software 7 and IBM SPSS Statistic 26. All continuous variables were represented as mean ± standard error of the mean (SEM), whereas categorical ones were represented in percentage (%). The comparison of data was carried out through non-parametric tests for comparisons between only two groups and analysis of variance (one-way ANOVA) with Tuckey correction for comparison between more than two groups. Further, a test for trends was performed to evaluate dose-response effects in the different groups regarding the stages of pathologies. The values of $p \leq 0.05$ were treated as statistically significant.

Acknowledgment

The authors thank the Cardiovascular Imaging Area and the Cardiovascular Surgery Area of the Centro Cardiologico Monzino IRCCS for echocardiographic data and specimen collection.

Authors' Contribution

P.P. and V.V. conceived and designed the study. G.K. and N.P. substantially contributed to the design of the work. V.V., G.K., D.M., and B.P. acquired the data. V.V. and I.M. analyzed the data. V.V., M.C., P.S., A.S.M., V.A., D.M., V.A.M., M.Z., N.P., and P.P. interpreted the data. V.V. drafted the work. G.K., B.P., M.C., I.M., P.S., A.S.M., V.A., D.M., V.A.M., M.Z., N.P., and P.P critically revised the work for important intellectual content. All the authors gave their final approval to the present version of the work, and all the authors agreed to be accountable for all aspects of the work.

Author Disclosure Statement

No competing financial interests exist.

Funding Information

This work was supported by the Italian Ministry of Health funds (Ricerca Finalizzata: GR-2018-12366423) and by Fondazione Gigi e Pupa Ferrari ONLUS (FPF-14). G.K. is supported by the T32 NIH training grant (T32AG058527) and funds from the Johns Hopkins University Older American Independence Center of the National Institute on Aging (NIA) under award number P30AG021334. NP is supported by NIH (R01 HL136918).

Supplementary Material

Supplementary Table S1
Supplementary Figure S1
Supplementary Figure S2
Supplementary Figure S3
Supplementary Figure S4
Supplementary Figure S5
Supplementary Figure S6
Supplementary Figure S7

References

1. Alushi B, Curini L, Christopher MR, Grubitzch H, Landmesser U, Amedei A, and Lauten A. Calcific Aortic Valve Disease-Natural History and Future Therapeutic Strategies. *Front Pharmacol* 11: 685, 2020.
2. Aruoma OI, Halliwell B, Hoey BM, and Butler J. The antioxidant action of N-acetylcysteine: its reaction with hydrogen peroxide, hydroxyl radical, superoxide, and hypochlorous acid. *Free Radic Biol Med* 6: 593–597, 1989.
3. Asensi M, Sastre J, Pallardo FV, Lloret A, Lehner M, Garcia-de-la Asuncion J, and Vina J. Ratio of reduced to oxidized glutathione as indicator of oxidative stress status and DNA damage. *Methods Enzymol* 299: 267–276, 1999.
4. Ates B, Abraham L, and Ercal N. Antioxidant and free radical scavenging properties of N-acetylcysteine amide (NACA) and comparison with N-acetylcysteine (NAC). *Free Radic Res* 42: 372–377, 2008.

5. Bajic VP, Van Neste C, Obradovic M, Zafirovic S, Radak D, Bajic VB, Essack M, and Isenovic ER. Glutathione ''Redox Homeostasis'' and Its Relation to Cardiovascular Disease. *Oxid Med Cell Longev* 2019: 5028181, 2019.
6. Bartekova M, Barancik M, Ferenczyova K, and Dhalla NS. Beneficial Effects of N-acetylcysteine and N-mercaptopropionylglycine on Ischemia Reperfusion Injury in the Heart. *Curr Med Chem* 25: 355–366, 2018.
7. Baumgartner H, Falk V, Bax JJ, De Bonis M, Hamm C, Holm PJ, Iung B, Lancellotti P, Lansac E, Rodriguez Munoz D, Rosenhek R, Sjogren J, Tornos Mas P, Vahanian A, Walther T, Wendler O, Windecker S, Zamorano JL, and Group ESCSD. 2017 ESC/EACTS Guidelines for the management of valvular heart disease. *Eur Heart J* 38: 2739–2791, 2017.
8. Bavarsad Shahripour R, Harrigan MR, and Alexandrov AV. N-acetylcysteine (NAC) in neurological disorders: mechanisms of action and therapeutic opportunities. *Brain Behav* 4: 108–122, 2014.
9. Behr J, Demedts M, Buhl R, Costabel U, Dekhuijzen RP, Jansen HM, MacNee W, Thomeer M, Wallaert B, Laurent F, Nicholson AG, Verbeken EK, Verschakelen J, Flower CD, Petruzzelli S, De Vuyst P, van den Bosch JM, Rodriguez-Becerra E, Lankhorst I, Sardina M, and Boissard G; group Is. Lung function in idiopathic pulmonary fibrosis—extended analyses of the IFIGENIA trial. *Respir Res* 10: 101, 2009.
10. Birben E, Sahiner UM, Sackesen C, Erzurum S, and Kalayci O. Oxidative stress and antioxidant defense. *World Allergy Organ J* 5: 9–19, 2012.
11. Branchetti E, Sainger R, Poggio P, Grau JB, Patterson-Fortin J, Bavaria JE, Chorny M, Lai E, Gorman RC, Levy RJ, and Ferrari G. Antioxidant enzymes reduce DNA damage and early activation of valvular interstitial cells in aortic valve sclerosis. *Arterioscler Thromb Vasc Biol* 33: e66–e74, 2013.
12. Chaves Cayuela N, Kiyomi Koike M, Jacysyn JF, Rasslan R, Azevedo Cerqueira AR, Pereira Costa SK, Picanco Diniz-Junior JA, Massazo Utiyama E, Frasson de Souza Montero E. N-acetylcysteine reduced ischemia and reperfusion damage associated with steatohepatitis in mice. *Int J Mol Sci* 21: 4106, 2020.
13. Chelko SP, Keceli G, Carpi A, Doti N, Agrimi J, Asimaki A, Beti CB, Miyamoto M, Amat-Codina N, Bedja D, Wei AC, Murray B, Tichnell C, Kwon C, Calkins H, James CA, O'Rourke B, Halushka MK, Melloni E, Saffitz JE, Judge DP, Ruvo M, Kitsis RN, Andersen P, Di Lisa F, and Paolocci N. Exercise triggers CAPN1-mediated AIF truncation, inducing myocyte cell death in arrhythmogenic cardiomyopathy. *Sci Transl Med* 13: eabf0891, 2021.
14. Chen CA, Wang TY, Varadharaj S, Reyes LA, Hemann C, Talukder MA, Chen YR, Druhan LJ, and Zweier JL. S-glutathionylation uncouples eNOS and regulates its cellular and vascular function. *Nature* 468: 1115–1118, 2010.
15. Costa DLC, Diniz JB, Requena G, Joaquim MA, Pittenger C, Bloch MH, Miguel EC, and Shavitt RG. Randomized, double-blind, placebo-controlled trial of N-acetylcysteine augmentation for treatment-resistant obsessive-compulsive disorder. *J Clin Psychiatry* 78: e766–e773, 2017.
16. Cui Y, Narasimhulu CA, Liu L, Zhang Q, Liu PZ, Li X, Xiao Y, Zhang J, Hao H, Xie X, He G, Cui L, Parthasarathy S, and Liu Z. N-acetylcysteine inhibits in vivo oxidation of native low-density lipoprotein. *Sci Rep* 5: 16339, 2015.
17. Danielsen R, Aspelund T, Harris TB, and Gudnason V. The prevalence of aortic stenosis in the elderly in Iceland and predictions for the coming decades: the AGES-Reykjavik study. *Int J Cardiol* 176: 916–922, 2014.
18. De Pascali F, Hemann C, Samons K, Chen CA, and Zweier JL. Hypoxia and reoxygenation induce endothelial nitric oxide synthase uncoupling in endothelial cells through tetrahydrobiopterin depletion and S-glutathionylation. *Biochemistry* 53: 3679–3688, 2014.
19. de Souza LF, Schmitz AE, da Silva LCS, de Oliveira KA, Nedel CB, Tasca CI, de Bem AF, Farina M, and Dafre AL. Inhibition of reductase systems by 2-AAPA modulates peroxiredoxin oxidation and mitochondrial function in A172 glioblastoma cells. *Toxicol In Vitro* 42: 273–280, 2017.
20. Emdin M, Pompella A, and Paolicchi A. Gamma-glutamyltransferase, atherosclerosis, and cardiovascular disease: triggering oxidative stress within the plaque. *Circulation* 112: 2078–2080, 2005.
21. Eshaq RS and Harris NR. Loss of Platelet Endothelial Cell Adhesion Molecule-1 (PECAM-1) in the diabetic retina: role of matrix metalloproteinases. *Invest Ophthalmol Vis Sci* 60: 748–760, 2019.
22. Farrar EJ, Huntley GD, and Butcher J. Endothelial-derived oxidative stress drives myofibroblastic activation and calcification of the aortic valve. *PLoS One* 10: e0123257, 2015.
23. Forman HJ, Zhang H, and Rinna A. Glutathione: overview of its protective roles, measurement, and biosynthesis. *Mol Aspects Med* 30: 1–12, 2009.
24. Freeman RV and Otto CM. Spectrum of calcific aortic valve disease: pathogenesis, disease progression, and treatment strategies. *Circulation* 111: 3316–3326, 2005.
25. Gebhart V, Reiss K, Kollau A, Mayer B, and Gorren ACF. Site and mechanism of uncoupling of nitric-oxide synthase: uncoupling by monomerization and other misconceptions. *Nitric Oxide* 89: 14–21, 2019.
26. Gharacholou SM, Karon BL, Shub C, and Pellikka PA. Aortic valve sclerosis and clinical outcomes: moving toward a definition. *Am J Med* 124: 103–110, 2011.
27. Ghezzi P. Protein glutathionylation in health and disease. *Biochim Biophys Acta* 1830: 3165–3172, 2013.
28. Giustarini D, Rossi R, Milzani A, Colombo R, Dalle-Donne I. S-glutathionylation: from redox regulation of protein functions to human diseases. *J Cell Mol Med* 8: 201–212, 2004.
29. Goto S, Rogers MA, Blaser MC, Higashi H, Lee LH, Schlotter F, Body SC, Aikawa M, Singh SA, and Aikawa E. Standardization of human calcific aortic valve disease in vitro modeling reveals passage-dependent calcification. *Front Cardiovasc Med* 6: 49, 2019.
30. Greenberg HZE, Zhao G, Shah AM, and Zhang M. Role of oxidative stress in calcific aortic valve disease and its therapeutic implications. *Cardiovasc Res* 2021 [Epub ahead of print]; DOI: 10.1093/cvr/cvab142.
31. Gupta SK, Kamendulis LM, Clauss MA, and Liu Z. A randomized, placebo-controlled pilot trial of N-acetylcysteine on oxidative stress and endothelial function in HIV-infected older adults receiving antiretroviral treatment. *AIDS* 30: 2389–2391, 2016.
32. Hamilton CA, Brosnan MJ, McIntyre M, Graham D, and Dominiczak AF. Superoxide excess in hypertension and aging: a common cause of endothelial dysfunction. *Hypertension* 37: 529–534, 2001.

33. Heard KJ. Acetylcysteine for acetaminophen poisoning. *N Engl J Med* 359: 285–292, 2008.
34. Hsu SP, Chiang CK, Yang SY, and Chien CT. N-acetylcysteine for the management of anemia and oxidative stress in hemodialysis patients. *Nephron Clin Pract* 116: c207–c216, 2010.
35. Hwang C, Sinskey AJ, and Lodish HF. Oxidized redox state of glutathione in the endoplasmic reticulum. *Science* 257: 1496–1502, 1992.
36. Jakic B, Buszko M, Cappellano G, and Wick G. Elevated sodium leads to the increased expression of HSP60 and induces apoptosis in HUVECs. *PLoS One* 12: e0179383, 2017.
37. Kalyanaraman B, Darley-Usmar V, Davies KJ, Dennery PA, Forman HJ, Grisham MB, Mann GE, Moore K, Roberts LJ, 2nd, and Ischiropoulos H. Measuring reactive oxygen and nitrogen species with fluorescent probes: challenges and limitations. *Free Radic Biol Med* 52: 1–6, 2012.
38. Keceli G, Gupta A, Sourdon J, Gabr R, Schar M, Dey S, Tocchetti CG, Stuber A, Agrimi J, Zhang Y, Leppo M, Steenbergen C, Lai S, Yanek LR, O'Rourke B, Gerstenblith G, Bottomley PA, Wang Y, Paolocci N, and Weiss RG. Mitochondrial creatine kinase attenuates pathologic remodeling in heart failure. *Circ Res* 130: 741–759, 2022.
39. Kumarswamy R, Volkmann I, Jazbutyte V, Dangwal S, Park DH, and Thum T. Transforming growth factor-beta-induced endothelial-to-mesenchymal transition is partly mediated by microRNA-21. *Arterioscler Thromb Vasc Biol* 32: 361–369, 2012.
40. Leopold JA. Cellular mechanisms of aortic valve calcification. *Circ Cardiovasc Interv* 5: 605–614, 2012.
41. Li X, Jiang Z, Feng J, Zhang X, Wu J, and Chen W. 2-Acetylamino-3-[4-(2-acetylamino-2-carboxyethylsulfanyl-carbonylamino) phenyl carbamoylsulfanyl] propionic acid, a glutathione reductase inhibitor, induces G2/M cell cycle arrest through generation of thiol oxidative stress in human esophageal cancer cells. *Oncotarget* 8: 61846–61860, 2017.
42. Lindman BR, Clavel MA, Mathieu P, Iung B, Lancellotti P, Otto CM, and Pibarot P. Calcific aortic stenosis. *Nat Rev Dis Primers* 2: 16006, 2016.
43. Miller JD, Chu Y, Brooks RM, Richenbacher WE, Pena-Silva R, and Heistad DD. Dysregulation of antioxidant mechanisms contributes to increased oxidative stress in calcific aortic valvular stenosis in humans. *J Am Coll Cardiol* 52: 843–850, 2008.
44. Miller JD, Weiss RM, Serrano KM, Castaneda LE, Brooks RM, Zimmerman K, and Heistad DD. Evidence for active regulation of pro-osteogenic signaling in advanced aortic valve disease. *Arterioscler Thromb Vasc Biol* 30: 2482–2486, 2010.
45. Nkomo VT, Gardin JM, Skelton TN, Gottdiener JS, Scott CG, Enriquez-Sarano M. Burden of valvular heart diseases: a population-based study. *Lancet* 368: 1005–1011, 2006.
46. Nsaibia MJ, Boulanger MC, Bouchareb R, Mkannez G, Le Quang K, Hadji F, Argaud D, Dahou A, Bosse Y, Koschinsky ML, Pibarot P, Arsenault BJ, Marette A, and Mathieu P. OxLDL-derived lysophosphatidic acid promotes the progression of aortic valve stenosis through a LPAR1-RhoA-NF-kappaB pathway. *Cardiovasc Res* 113: 1351–1363, 2017.
47. Otto CM, Lind BK, Kitzman DW, Gersh BJ, and Siscovick DS. Association of aortic-valve sclerosis with cardiovascular mortality and morbidity in the elderly. *N Engl J Med* 341: 142–147, 1999.
48. Otto CM and Prendergast B. Aortic-valve stenosis—from patients at risk to severe valve obstruction. *N Engl J Med* 371: 744–756, 2014.
49. Parfenova H, Basuroy S, Bhattacharya S, Tcheranova D, Qu Y, Regan RF, and Leffler CW. Glutamate induces oxidative stress and apoptosis in cerebral vascular endothelial cells: contributions of HO-1 and HO-2 to cytoprotection. *Am J Physiol Cell Physiol* 290: C1399–C1410, 2006.
50. Pastore A and Piemonte F. Protein glutathionylation in cardiovascular diseases. *Int J Mol Sci* 14: 20845–20876, 2013.
51. Pazianas M. Calcific aortic stenosis. *N Engl J Med* 360: 85; author reply 85–86, 2009.
52. Peeters F, Meex SJR, Dweck MR, Aikawa E, Crijns H, Schurgers LJ, and Kietselaer B. Calcific aortic valve stenosis: hard disease in the heart: a biomolecular approach towards diagnosis and treatment. *Eur Heart J* 39: 2618–2624, 2018.
53. Perrucci GL, Zanobini M, Gripari P, Songia P, Alshaikh B, Tremoli E, and Poggio P. Pathophysiology of aortic stenosis and mitral regurgitation. *Compr Physiol* 7: 799–818, 2017.
54. Poggio P, Songia P, Moschetta D, Valerio V, Myasoedova V, Perrucci GL, and Pompilio G. MiRNA profiling revealed enhanced susceptibility to oxidative stress of endothelial cells from bicuspid aortic valve. *J Mol Cell Cardiol* 131: 146–154, 2019.
55. Popov D. Protein S-glutathionylation: from current basics to targeted modifications. *Arch Physiol Biochem* 120: 123–130, 2014.
56. Prasain N and Stevens T. The actin cytoskeleton in endothelial cell phenotypes. *Microvasc Res* 77: 53–63, 2009.
57. Rajamannan NM, Bonow RO, and Rahimtoola SH. Calcific aortic stenosis: an update. *Nat Clin Pract Cardiovasc Med* 4: 254–262, 2007.
58. Reyes DRA, Gomes MJ, Rosa CM, Pagan LU, Damatto FC, Damatto RL, Depra I, Campos DHS, Fernandez AAH, Martinez PF, Okoshi K, and Okoshi MP. N-acetylcysteine influence on oxidative stress and cardiac remodeling in rats during transition from compensated left ventricular hypertrophy to heart failure. *Cell Physiol Biochem* 44: 2310–2321, 2017.
59. Rocha M, Apostolova N, Hernandez-Mijares A, Herance R, and Victor VM. Oxidative stress and endothelial dysfunction in cardiovascular disease: mitochondria-targeted therapeutics. *Curr Med Chem* 17: 3827–3841, 2010.
60. Sider KL, Blaser MC, and Simmons CA. Animal models of calcific aortic valve disease. *Int J Inflam* 2011: 364310, 2011.
61. Sies H. Glutathione and its role in cellular functions. *Free Radic Biol Med* 27: 916–921, 1999.
62. Songia P, Branchetti E, Parolari A, Myasoedova V, Ferrari G, Alamanni F, Tremoli E, and Poggio P. Mitral valve endothelial cells secrete osteoprotegerin during endothelial mesenchymal transition. *J Mol Cell Cardiol* 98: 48–57, 2016.
63. Squellerio I, Caruso D, Porro B, Veglia F, Tremoli E, and Cavalca V. Direct glutathione quantification in human blood by LC-MS/MS: comparison with HPLC with electrochemical detection. *J Pharm Biomed Anal* 71: 111–118, 2012.
64. Stanley BA, Sivakumaran V, Shi S, McDonald I, Lloyd D, Watson WH, Aon MA, and Paolocci N. Thioredoxin

reductase-2 is essential for keeping low levels of H(2)O(2) emission from isolated heart mitochondria. *J Biol Chem* 286: 33669–33677, 2011.
65. Subrahmanian S, Varshney R, Subramani K, Murphy B, Woolington S, and Ahamed J. N-acetylcysteine inhibits aortic stenosis progression in a murine model by blocking shear-induced activation of platelet latent transforming growth factor beta 1. *Antioxid Redox Signal* 2021 [Epub ahead of print]; DOI: 10.1089/ars.2021.0037.
66. Summerhill VI, Moschetta D, Orekhov AN, Poggio P, and Myasoedova VA. Sex-specific features of calcific aortic valve disease. *Int J Mol Sci* 21: 5620, 2020.
67. Tepel M, van der Giet M, Statz M, Jankowski J, and Zidek W. The antioxidant acetylcysteine reduces cardiovascular events in patients with end-stage renal failure: a randomized, controlled trial. *Circulation* 107: 992–995, 2003.
68. Valerio V, Myasoedova VA, Moschetta D, Porro B, Perrucci GL, Cavalca V, Cavallotti L, Songia P, and Poggio P. Impact of oxidative stress and protein S-glutathionylation in aortic valve sclerosis patients with overt atherosclerosis. *J Clin Med* 8: 552, 2019.
69. VanHecke GC, Abeywardana MY, and Ahn YH. Proteomic Identification of Protein Glutathionylation in Cardiomyocytes. *J Proteome Res* 18: 1806–1818, 2019.
70. Xiong Y, Uys JD, Tew KD, and Townsend DM. S-glutathionylation: from molecular mechanisms to health outcomes. *Antioxid Redox Signal* 15: 233–270, 2011.
71. Xu K, Xie S, Huang Y, Zhou T, Liu M, Zhu P, Wang C, Shi J, Li F, Sellke FW, and Dong N. Cell-type transcriptome atlas of human aortic valves reveal cell heterogeneity and endothelial to mesenchymal transition involved in calcific aortic valve disease. *Arterioscler Thromb Vasc Biol* 40: 2910–2921, 2020.
72. Zafarullah M, Li WQ, Sylvester J, and Ahmad M. Molecular mechanisms of N-acetylcysteine actions. *Cell Mol Life Sci* 60: 6–20, 2003.
73. Zeisberg EM, Potenta S, Xie L, Zeisberg M, and Kalluri R. Discovery of endothelial to mesenchymal transition as a source for carcinoma-associated fibroblasts. *Cancer Res* 67: 10123–10128, 2007.
74. Zhao Y, Seefeldt T, Chen W, Wang X, Matthees D, Hu Y, and Guan X. Effects of glutathione reductase inhibition on cellular thiol redox state and related systems. *Arch Biochem Biophys* 485: 56–62, 2009.
75. Zitka O, Skalickova S, Gumulec J, Masarik M, Adam V, Hubalek J, Trnkova L, Kruseova J, Eckschlager T, and Kizek R. Redox status expressed as GSH:GSSG ratio as a marker for oxidative stress in paediatric tumour patients. *Oncol Lett* 4: 1247–1253, 2012.

Address correspondence to:
Dr. Paolo Poggio
Unità per lo Studio delle Patologie Aortiche
Valvolari e Coronariche
Centro Cardiologico Monzino IRCCS
Via privata Carlo Parea, 4
Milan 20138
Italy

E-mail: paolo.poggio@cardiologicomonzino.it

Date of first submission to ARS Central, June 22, 2021; date of final revised submission, April 7, 2022; date of acceptance, April 11, 2022.

Abbreviations Used

2-AAPA = 2-acetylamino-3-[4-(2-acetylamino-2-carboxyethylsulfanylthiocarbonylamino)-phenylthiocarbamoylsulfanyl]propionic acid
AS = aortic stenosis
AVR = aortic valve replacement
AVSc = aortic valve sclerosis
CAVS = calcific aortic valve stenosis
EPR = electron paramagnetic resonance
eNOS = endothelial nitric oxide synthase
GR = glutathione reductase
hVEC = human VEC
LC-MS/MS = liquid chromatography-tandem mass spectrometry
LDLR = low-density lipoprotein receptor
MMP2 = metalloproteinase type 2
MRM = multiple reaction monitoring
NAC = N-acetyl-L-cysteine
P-SSG = protein S-glutathionylation
pVEC = porcine VEC
ROS = reactive oxygen species
TIMP2 = tissue inhibitor of metalloproteinase 2
VEC = valve endothelial cell
VIC = valve interstitial cell